



Multistage pervasive fluid–rock interactions and Hf mobility in deeply subducted continental crust, Dabie terrane, eastern China

Penghui Chen¹ · Penglei Liu¹ · Zhenmin Jin¹

Received: 2 April 2024 / Accepted: 3 July 2024 / Published online: 19 July 2024
© The Author(s), under exclusive licence to Springer-Verlag GmbH Germany, part of Springer Nature 2024

Abstract

Garnet and zircon in a marble-hosted eclogite from the Dabie ultrahigh-pressure (UHP) terrane, eastern China record a wealth of information on multistage pervasive fluid–rock interactions and Hf mobility in deep continental subduction zones. The eclogite has a peak mineral assemblage of garnet + omphacite + phengite + coesite + magnesite ± dolomite + rutile. Five (inner patchy core, outer core, mantle, inner rim, outer rim) compositional zones were recognized for garnet. According to phase equilibria modeling, the inner patchy and outer cores of garnet likely document a prograde breakdown of lawsonite to UHP peak (3.0–4.5 GPa and 630–750 °C), while a Ca-metasomatism could have also played a role in their formation. The other three garnet zones resulted from multistage garnet re-equilibration at eclogite-facies conditions during isothermal exhumation. The stepwise compositional changes between these different garnet zones suggest that dissolution and reprecipitation played a key role in the garnet re-equilibration, while the repeated actions of such a re-equilibration mechanism reflect multistage pervasive fluid–rock interactions. Zircon from the rock develops three eclogite-facies domains (1, 2, 3). Textural relationships suggest that domain 2 formed in between domain 1 and 3. LA-ICP-MS analyses yielded ²⁰⁶Pb/²³⁸U ages of 233 ± 6 Ma, 232 ± 2 Ma and 222 ± 3 Ma for domain 1, 2 and 3, respectively. Domain 1 includes coesite and magnesite and its Th/U is usually higher than 0.1. This domain is interpreted to have formed in the absence of allanite during prograde UHP metamorphism. Domain 2 shows slightly lower Σ MREEs (middle rare earth elements; 7.5–13.5 ppm) and lower Ti (3.0–6.0 ppm) contents than domain 1 (Σ MREEs = 10.5–21.0 ppm; Ti = 4.5–7.0 ppm) and most likely formed at the UHP peak. Domain 3 contains much lower Σ MREEs (3.5–6.0 ppm) and higher Ti (7.5–11.0 ppm) contents than domain 1 and 2, which is interpreted to have formed in the stability field of epidote during decompression. Domain 2 (0.282354–0.282607) and 3 (0.282449–0.282636) display lower initial ¹⁷⁶Hf/¹⁷⁷Hf values than domain 1 (0.282563–0.282667), suggesting that external fluids introduced Hf into the eclogite. These findings not only shed new light on the flow mode of fluids and their role in resetting mineral compositions in deep subduction zones, but also suggest that Hf (a key high-field strength and tracer element) can be efficiently mobilized by (U)HP fluids. Moreover, this study highlights the influence of epidote-group minerals and pressure on the chemistry (Th/U ratio and REE and Ti contents) of zircon.

Keywords UHP · Eclogite · Garnet · Zircon · Hf mobility · Fluid–rock interactions

Introduction

Fluids modulate many geodynamic processes in deep subduction zones, such as metamorphic reactions (e.g. Carlson et al. 2000; Guiraud et al. 2001; Proyer 2003) and

geochemical recycling (e.g. Hermann et al. 2006; Spandler and Pirard 2013). The release of fluids is mainly related to dehydration reactions in descending slabs, and experimental and thermodynamic modeling studies have provided a framework of devolatilization regimes for subducted rocks (e.g. Massonne 2009; Schmidt and Poli 1998; Wei and Duan 2018). Nonetheless, the nature of fluid activities in descending slabs and the role of deep fluids in element transfer remain unclear in many aspects.

There are two basic modes of fluid flow (i.e. pervasive and channelized flow) in deep subduction zones (Ague 2014). Channelized flow is defined as fluids being focused

Communicated by Othmar Müntener.

✉ Penglei Liu
liupenglei@cug.edu.cn

¹ School of Earth Sciences, China University of Geosciences, Wuhan 430074, China

into a highly strained or a lithologic contact zone where the high permeability allows efficient fluid migration. Fluid flow in this way can easily cause the alteration of local bulk-rock composition because of the high fluid–rock ratio in a confined environment (e.g. Guo et al. 2012; Hoover et al. 2022; John et al. 2008). By contrast, pervasive flow allows fluids to equilibrate with the rock matrix pervasively due to fluid migration along grain boundaries and microfractures in a bulk rock with low permeability (e.g. Bovay et al. 2021; Liu et al. 2017; Vho et al. 2020). In favorable cases, new minerals formed by consuming early minerals, leaving evidence of pervasive fluid flow easily recognized (e.g. Guo et al. 2022; Massonne 2012; Zeh and Gerdes 2014). In other cases, early minerals were only partly altered for their compositions and no new minerals formed (e.g. Bovay et al. 2021; Liu et al. 2017; Nosenzo et al. 2023). Alternatively, all the early minerals could have been totally replaced, and only a bulk-rock chemical fingerprint was left (e.g. Gao et al. 2019; Xiong et al. 2021). Partly because of crypticity, pervasive flow has received much less attention than channelized flow. Also noted is that dissolution and reprecipitation play a key role in altering mineral compositions during pervasive fluid–rock interactions (Martin et al. 2011; Putnis and Mezger 2004; Smit et al. 2008).

Since pervasive fluid–rock interactions are more challenging to decode, a more targeted mineral and approach is required. Garnet, a mineral that has been widely used to reconstruct pressure–temperature–time (P–T–t) paths, can also record key information on fluid–rock interactions (e.g. Bovay et al. 2021; Giuntoli et al. 2018; Vho et al. 2020). In response to fluid–rock interactions, the garnet composition can get partly reset via fluid-aided dissolution and reprecipitation (Cheng et al. 2007; Martin et al. 2011). In addition, microfractures in garnet have been shown to be efficient fluid-mediated transport channels for element exchange between the garnet interiors and matrix and/or for the dissolution of former garnet cores, leaving fingerprints such as healed fractures and atoll grains (Bovay et al. 2021; Giuntoli et al. 2018; Vho et al. 2020). Accordingly, a detailed study of garnet chemistry and texture can help reconstruct both the P–T–t path and fluid evolution of the host rock.

Metamorphic zircons are another good indicator of fluid–rock interactions as their formation are usually aided by fluids (Corfu et al. 2003; Rubatto and Hermann 2003; Zheng et al. 2004). Metamorphic zircons commonly display a Th/U ratio lower than 0.1, which likely reflects the compositional influence of coexisting allanite (and/or monazite; Rubatto et al. 2009; Stepanov et al. 2016). Epidote-group minerals are also known to be rich in light and middle rare earth elements (LREEs and MREEs). Their growth may exert a control on the contents of LREE and MREE in metamorphic zircons. However, such a correlation has been rarely demonstrated in literature. Meanwhile, the content of

Ti in zircon is positively correlated with temperature (Ferry and Watson 2007; Watson et al. 2006). Thus, the increase of Ti contents in zircon has been often used as an indicator of prograde metamorphism (e.g. Chen et al. 2013; Gao et al. 2011; Stepanov et al. 2016). In fact, pressure also exerts a control on the Ti content in zircon (Ferriss et al. 2008; Tailby et al. 2011), which has to be considered when interpreting the formation of zircons in UHP rocks that traveled through a large pressure window (Liu and Jin 2022).

A key question related to pervasive fluid–rock interactions is the origin of fluids, which can be either internally or externally derived. Oxygen isotopes in garnet and zircon have been widely used to constrain the origin of metasomatic fluids (e.g. Bovay et al. 2021; Chen et al. 2011). Whether Hf isotopes in zircon can be used as an efficient fluid tracer remains to explore and relevant successful applications have been rarely reported in literature (Zeh and Gerdes 2014). Answering this question also bears important implications for the mobility of Hf, a key high field-strength element (HFSE). Hafnium has a very low solubility in aqueous fluids (Ayers and Watson 1991; Kovalenko and Ryzhenko 2009; Schmidt et al. 2006), which has been commonly invoked as an explanation for the preservation of initial Hf isotopes in fluid-aided recrystallized zircons (Chen et al. 2010; Gerdes and Zeh 2009; Lenting et al. 2010). However, the occurrences of zircon in (ultra)high-pressure ((U)HP) veins require a new understanding of the behavior of Hf (and Zr) in deep fluids (Chen et al. 2012; Zheng et al. 2007). Experimental studies have demonstrated that Na–Al–silicate-bearing and alkaline CaCl_2 solutions can dissolve considerable Zr (up 1000 ppm) in the form of alkali zircon-silicate and $\text{Ca}_3[\text{Zr}(\text{OH})_6]^{4+}$ complexes, respectively (Brendebach et al. 2007; Wilke et al. 2012). It can be thus inferred that Hf (an analogue of Zr given the similar ionic charges and radii) can be used as a fluid tracer in favorable situations.

In this study, a marble-hosted eclogite from the Dabie UHP terrane was subjected to a detailed study. Garnet and zircon in the eclogite develop complicated zoning patterns and record multistage pervasive fluid–rock interactions. In combination of phase equilibria modeling and zircon geochronology, the P–T–t–fluid evolution of the eclogite was reconstructed. Importantly, zircon Hf isotopic studies provided a key constraint on the fluid source. At the meantime, the role of epidote-group minerals and pressure in determining the zircon chemistry (Th/U ratio and LREE–MREE–Ti contents) were highlighted.

Geological setting

The Dabie–Sulu orogenic belt contains one of the largest UHP metamorphic terranes in the world and is characterized by well-preserved coesite-bearing eclogites (e.g. Carswell

et al. 1997; Guo et al. 2012; Li et al. 2004; Liu et al. 2019). It lies in the eastern part of the Qinling–Dabie–Sulu orogenic belt (Fig. 1a) and resulted from northward subduction of the South China Block beneath the North China Block during the Triassic (e.g. Cong 1996; Hacker et al. 1998; Zheng et al. 2003). The Dabie and Sulu terranes are separated by the Tanlu fault with a sinistral displacement of about 550 km (Fig. 1a). The Dabie terrane to the west is further truncated by the NS-trending Shangma fault, the western and eastern segments of which are known as the Hongan (or western Dabie) and eastern Dabie terrane, respectively (Fig. 1a). The eastern Dabie terrane are separated by a series of large-scale EW-trending faults into five major litho-tectonic units with distinct metamorphic grades (Fig. 1a). From north to south, these five units are (1) the Beihuaiyang greenschist-facies zone, (2) the North Dabie granulite-facies and migmatitic zone, (3) the Central Dabie medium-T/UHP eclogite-facies zone (CDZ), (4) the South Dabie low-T eclogite-facies zone, and (5) the Susong blueschist-facies zone (Zheng et al. 2005a). All these five units are intruded by Early Cretaceous granitoids that resulted from the anatexis of thickened orogenic lithospheric keel during the collapse of the orogen (Chen et al. 2002; Zhang et al. 2002).

As shown in Fig. 1b, the CDZ includes three major lithological units: ortho- and para-gneiss, granitic gneiss, and marble-paragneiss units (Baker et al. 1997; Liu et al. 2003; Rolfo et al. 2004). The ortho- and para-gneiss unit is mainly composed of mica-plagioclase gneisses and schists, whereas the granitic gneiss unit mainly of two-feldspar granitic gneisses. The marble-paragneiss unit consists of paragneiss, marble, calc-silicate rock, schist, and jadeite quartzite and represents a supracrustal metasedimentary sequence. Eclogites, occurring as lenses, pods or layers within gneisses, marbles, and mafic–ultramafic complexes, are widespread in the ortho- and para-gneiss and marble-paragneiss units but absent in the granitic gneiss unit (Liu et al. 2003; and references therein). Inclusions of coesite and its pseudomorph have been found in nearly all the rock types (e.g. eclogite, marble, jadeite quartzite, and paragneiss) in the marble-paragneiss unit (e.g. Cong et al. 1995; Liu et al. 2001; 2015, 2017; Okay et al. 1989; Rolfo et al. 2004; Wang and Liou 1993). The UHP P–T conditions have been estimated by many studies using conventional geothermobarometry and forward modelling, which are > 3 GPa and 650–750 °C (e.g. Carswell et al. 1997, 2000; Liu et al. 2015; Schmid et al. 2000; Wei et al. 2013). The period of UHP metamorphism has been well constrained by U–Pb dating on coesite-bearing zircons, with three main episodes of zircon growth identified at 241 Ma, 233 Ma, and 227 Ma, respectively (Liu et al. 2006a; Wu et al. 2006; Zheng et al. 2009). The Dabie UHP rocks experienced a two-stage exhumation (Li et al. 1993, 2000; Zheng et al. 2003). The early exhumation to the lower and/or middle crustal level was nearly isothermal

and relatively fast, with an exhumation rate of 3–10 mm per year (Liu and Liou 2011; Liu et al. 2006b; Wu et al. 2011).

The protoliths of most Dabie–Sulu UHP rocks formed in a continental rift setting to the north margin of the South China Block in the middle Neoproterozoic, in response to the breakup of the supercontinent Rodinia (Hacker et al. 1998; Zhang et al. 2009; Zheng et al. 2008). Extensive meteoric hydrothermal alterations had led the protoliths to obtain negative $\delta^{18}\text{O}$ values before subduction (Zheng et al. 2003). The preservation of such an isotopic signature in the rocks suggests limited mass exchange between the subducted slab and mantle during subduction and exhumation (Rumble et al. 2000; Zhang et al. 2009; Zheng et al. 2003). Nonetheless, fluid flow was still active within the subducted slab at mantle depths, as recorded by various (U)HP veins (e.g. Chen et al. 2012; Guo et al. 2012; Liu et al. 2019; Zhang et al. 2008; Zheng et al. 2007). The vein-forming fluids were generally locally sourced (Li et al. 2001; Zhao et al. 2016; Zheng et al. 2007), suggesting short distances of fluid migration via channelized flow. By contrast, evidence for pervasive (U)HP fluid flow has been documented much less for the Dabie–Sulu UHP rocks. Garnet Lu–Hf (Schmidt et al. 2008) and Sm–Nd (An et al. 2018) dating results indicate that the Dabie–Sulu UHP eclogites could have experienced extensive pervasive fluid–rock interactions during early exhumation. This has also been proposed for the Dabie impure marbles and jadeite quartzites based on the studies of Sr and Mg isotopes (Gao et al. 2019; Wawrzenitz et al. 2019). In addition, studies on mineral chemistry and phase equilibria modelling revealed two episodes of pervasive and cryptic fluid–rock interactions in the Dabie impure marbles and marble-hosted eclogites during early exhumation (Liu et al. 2017, 2019). Different to the vein-forming fluids, an external origin was usually proposed for the fluids responsible for the pervasive fluid–rock interactions (e.g. Gao et al. 2019; Liu et al. 2017, 2019; Massonne 2012; Schmidt et al. 2008; Wawrzenitz et al. 2019). The fluids could have been sourced from either a crustal (Gao et al. 2019; Liu et al. 2017; Massonne 2012) or a mantle (Wawrzenitz et al. 2019) reservoir.

Sample description

The eclogite (GJL10-8; GPS coordinates: 30°38'41.9"N, 116°19'37.4"E) studied here was collected from the Ganjialing area in the marble-paragneiss unit (Fig. 1b). It appears as a decimeter-sized block in impure marbles that exhibit compositional layers with different contents of silicate minerals and colors (Fig. 1c; Liu et al. 2015). Its contact to the host marble is sharp and characterized by a thin retrograde amphibolite rim after the eclogite. Many HP veins occur in this area and include quartz-, mica-, amphibole-, calcite-, and epidote-rich varieties (Liu et al. 2015). Interstitial

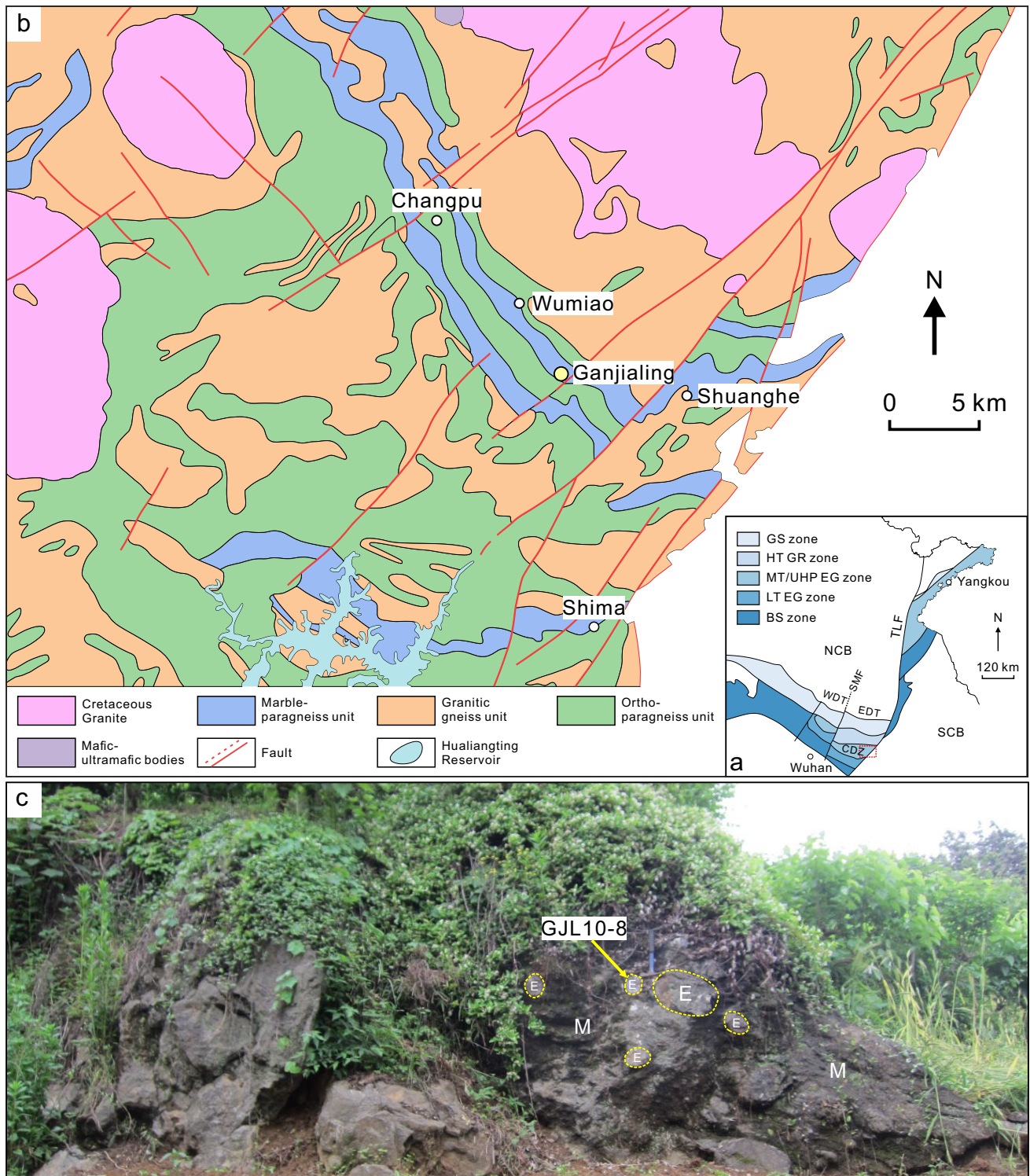


Fig. 1 **a** Sketch map of the Dabie–Sulu orogenic belt, showing the lithotectonic zones of distinct metamorphic grades (modified after Zheng et al. 2005a). **b** Geological map of the Central Dabie Zone (CDZ; modified after Liu et al. 2003). The sample locality (Ganjialing) is marked with a yellow circle. **c** Photograph of sampled out-

crop at Ganjialing. *GS* Greenschist facies; *GR* Granulite facies; *EG* Eclogite facies; *BS* Blueschist facies; *HT* high temperature; *LT* low temperature; *NCB* North China Block; *SCB* South China Block; *WDT* Western Dabie Terrane; *EDT* Eastern Dabie Terrane; *SMF* Shangma Fault; *TLF* Tanlu Fault; *M* Marble; *E* Eclogite

coesite and abundant coesite inclusions were found in rocks from the Ganjialing area and the peak UHP P–T conditions have been constrained at 4–4.5 GPa and 750 ± 50 °C (Liu et al. 2015, 2019).

Sample GJL10-8 is fine- to medium-grained and retrogressed to a medium degree. It consists of mainly garnet, omphacite, amphibole, phengite, clinozoisite, dolomite, and quartz/coesite (in order of content). Minor and accessory minerals include biotite, plagioclase, magnesite, calcite, rutile, titanite, zircon, and apatite. Garnet (0.2–2.0 mm) is idioblastic to xenoblastic and often forms clusters (Fig. 2a, b). Inclusions of omphacite, rutile, apatite, and coesite occur in garnet. Omphacite (0.2–2.0 mm) is generally hypidioblastic and partly replaced by a symplectite of diopside + amphibole + plagioclase (Fig. 2c, d). It contains inclusions of garnet, rutile, apatite, and coesite (Fig. 2a). Phengite (0.5–2.5 mm) includes small garnet blasts and can be partly replaced by a symplectite of biotite + plagioclase (Fig. 2c, d). Retrograde amphibole and clinozoisite occur either as coronae around garnet and omphacite or as hypidioblasts and xenoblasts (Fig. 2b–f). Noted is that some clinozoisite grains contain an allanite core (Fig. 2e). Dolomite is the main carbonate mineral and generally rimmed by calcite (Fig. 2f). Magnesite was only found in zircon. Rutile is partially or completely replaced by titanite (Fig. 2b).

Analytical methods

Analysis of bulk-rock composition

The bulk-rock composition was determined by X-ray fluorescence (XRF) on a fused glass disk at the State Key Laboratory of Geological Processes and Mineral Resources (GPMR), China University of Geosciences (CUG), Wuhan. The loss-on-ignition (LOI) was obtained from the weight loss after heating the dried rock powder at 1000 °C for 90 min. A Shimadzu XRF-1800 sequential X-ray fluorescence spectrometer was used for XRF analyses, with working conditions of 40 kV voltage and 70 mA current. Accuracy and precision monitored by analyses of USGS standard BHVO-2 and repeated samples were better than 3% and 1%, respectively. The measured bulk-rock composition is given in Table S1.

Analyses and X-ray mapping of mineral major elements

The analyses of major elements of minerals were completed by using two electron probe microanalyzers (EPMA) at the Center for Global Tectonic (CGT), School of Earth Sciences, CUG, Wuhan and at the Institut für Mineralogie und Kristallchemie (IMK), Universität Stuttgart. At the CGT,

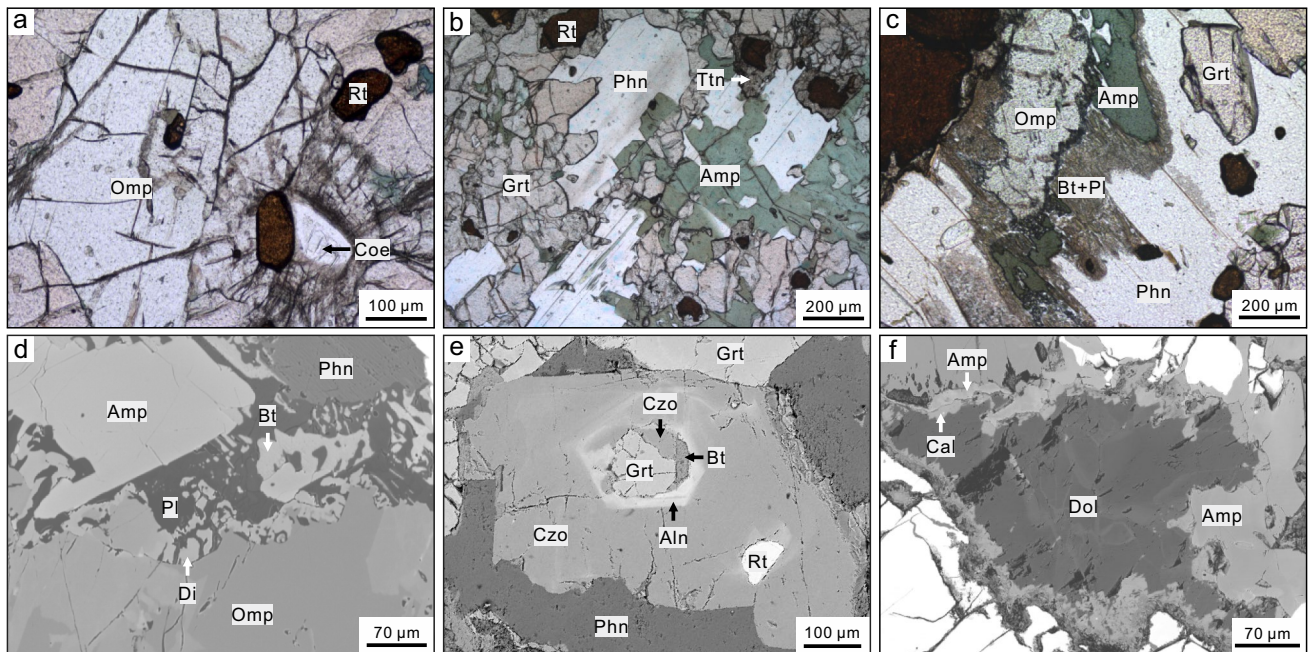


Fig. 2 Photomicrographs and back-scattered electron (BSE) images of eclogite GJL10-8. **a** Inclusion of coesite partly replaced by polycrystalline quartz in omphacite. Plane polarized light (PPL). **b** Phengite in textural equilibrium with garnet. Note that the rutile was partly replaced by titanite. PPL. **c** Symplectite of biotite + plagioclase after zoned omphacite and phengite. PPL. **d** Symplectites of diopside + amphibole + plagioclase

and biotite + plagioclase after zoned omphacite and phengite, respectively. BSE. **e** Zoned clinozoisite/allanite containing inclusions of garnet, biotite, clinozoisite, and rutile. BSE. **f** Zoned dolomite rimmed by calcite and amphibole. BSE. Mineral abbreviations are after Warr (2021) except for *phn* phengite

a JEOL JXA-8230 EPMA with four wavelength-dispersive spectrometers (WDS) were used. The working conditions were 15 kV accelerating voltage, 20 nA beam current, 1–10 μm beam diameter, and 10–20 s counting times. Raw X-ray intensities were corrected using a ZAF correction procedure and calibrated against a series of natural and synthetic SPI standards. Analyses at the IMK were performed using a CAMECA SX100 EPMA with five WDS. The working conditions were like those used at the CGT except that the beam current was 10–15 nA. Matrix correction was conducted by the PaP procedure provided by CAMECA. Natural and synthetic minerals and oxides were used as standards. Major element compositions of minerals are given in Tables S2–S8.

Elemental mapping was performed using the above two EPMA. The operating conditions for the JXA-8230 EPMA were 15 kV accelerating voltage, 100 nA beam current, 5 μm step width and 10 ms dwell time, while those for the CAMECA SX100 EPMA were 15 kV accelerating voltage, 20 nA beam current, 3 μm step width and 10 ms dwell time.

Analyses of garnet trace elements

The analyses of trace elements of garnet were conducted in thin sections by laser ablation inductively coupled plasma mass spectrometry (LA-ICP-MS) at GPMR, CUG, Wuhan. A GeoLas 2005 laser ablation system and an Agilent 7900 ICP-MS instrument were used for laser sampling and to acquire ion-signal intensities, respectively. Helium was used as the carrier gas and mixed with Argon (makeup gas) via a T-connector before entering the ICP. Nitrogen was introduced into the central gas flow (Ar + He) of the Ar plasma to improve the detection limits and the precision (Hu et al. 2008). A spot size of 32 μm and a laser frequency of 6 Hz were used. For each analysis, the Agilent Chemstation was applied to incorporate a background acquisition of 20–25 s followed by a 50 s acquisition from the sample. Off-line selection, integration of background and analytical signals and time-drift correction and quantitative calibration were carried out by the Excel software ICPMSDataCal (Liu et al. 2008, 2010). Element abundances were calibrated against reference materials of BIR-1G, BCR-2G and BHVO-2G without using an internal standard (Liu et al. 2008). Analyses of reference standards show that the precision and the accuracy (1σ) are better than 10% for trace elements (and 2% for major elements). Garnet trace element composition is given in Table S9.

Zircon cathodoluminescence (CL) imaging

Zircon grains from GJL10-8 were separated by magnetic and heavy liquid techniques and hand-picked under a binocular microscope. Separated zircon grains were mounted

in epoxy resin and polished down to the grain center. Two zircon mounts were prepared. One zircon mount was imaged by a Gatan Mono CL⁴⁺ cathodoluminescence system fitting on a FEI Quanta 450 field emission gun scanning electron microscope (SEM) at the GPMR, CUG, Wuhan. The imaging conditions were 10 kV accelerating voltage, 5 mm spot size, and 14 mm working distance. The other zircon mount was imaged at the Wuhan Sample Solution Analytical Technology Co., Ltd., Wuhan, China, using an Analytical SEM (JSM-IT300) connected to a Delmic sparc system. The imaging conditions were 0.5–30 kV voltage of electric field and 72 μA current of tungsten filament.

Identification of mineral inclusions in zircon

Mineral inclusions in zircon were identified using a Renishaw RM-1000 Raman spectrometer (532 nm line of an Ar⁺ laser) at the GPMR, CUG, Wuhan and a Renishaw inVia Raman spectrometer (514.5 nm line of an Ar⁺ laser) at the State Key Laboratory of Continental Dynamics, Northwest University, China. The 520 cm^{-1} signal generated by a monocrystalline Si wafer was used for calibrating both spectrometers. Mineral inclusions exposed at the surface were also identified using an Oxford INCA-X-Max 50 energy dispersive spectrometer fitting on a FEI Quanta 450 field emission gun SEM at the GPMR, CUG, Wuhan. The working conditions were 20 kV accelerating voltage, 5 mm spot size, and 12 mm working distance.

Analyses of zircon U–Pb and Lu–Hf isotopes

Analyses of U–Pb isotopes and trace elements of zircon were conducted synchronously by LA-ICP-MS. One zircon mount was analyzed at the GPMR, CUG, Wuhan. A GeoLas 2005 laser ablation system and an Agilent 7900 ICP-MS instrument were used for laser sampling and to acquire ion-signal intensities, respectively. The other zircon mount was analyzed with a GeolasPro laser ablation system and an Agilent 7900 ICP-MS at the Wuhan Sample Solution Analytical Technology Co., Ltd., Wuhan, China. Both laser ablation systems include a “wire” signal smoothing device. The working conditions were nearly identical at these two laboratories. Helium was used as the carrier gas and mixed with Argon (makeup gas) via a T-connector before entering the ICP. A spot size of 32 μm and a laser frequency of 5 Hz were used. Each analysis included a background acquisition of approximately 20–30 s followed by 50 s of data acquisition for the sample. Zircon standard GJ-1, Plesovice and Tanz were analyzed as unknowns. External standards used for U–Pb dating and trace element calibration were zircon 91,500 and glass NIST610, respectively. The external precision (2σ) of 91,500 is better than 2%. The pooled concordant ages of the secondary reference GJ-1 (recommended value:

608.5 ± 1.5 Ma; Jackson et al. 2004), Plešovice (recommended value: 337.1 ± 0.4 Ma; Sláma et al. 2008); and Tanz (recommended value: 566.16 ± 0.77 Ma; Hu et al. 2021) are 604 ± 3 Ma, 336 ± 4 Ma and 566 ± 5 Ma respectively. Detailed operating conditions for the laser ablation system and the ICP-MS instrument can be found in Liu et al. (2008) and Zong et al. (2017).

Hafnium isotopic ratios of zircon were determined with a Neptune Plus multiple collection ICP-MS equipped with a Geolas HD excimer ArF laser ablation system at the Wuhan Sample Solution Analytical Technology Co., Ltd., Wuhan, China. A “wire” signal smoothing device is included in this laser ablation system. Helium was utilized as the carrier gas and mixed with argon (makeup gas) after flowing out the ablation cell. Small amounts of N₂ were added to the argon makeup gas flow to improve the sensitivity of Hf isotopes. A single spot ablation mode (spot size 44 μm) was applied, and the energy density of laser ablation was ~ 7.0 J cm⁻². The signal acquisition was set to 20 s for the background and 50 s for the sample. Zircon Plešovice was used as an external standard for calibration. Zircon 91,500 and GJ-1 were used as the second standards to monitor the quality of data correction. The external precisions (2σ) of the three international zircon standards are better than 0.000025 (¹⁷⁶Hf/¹⁷⁷Hf). The test values are consistent with the recommended values within the error ranges. More details on the analytical conditions and procedures can be found in Hu et al. (2012).

Raw data of trace elements and U–Pb and Hf isotopes were processed by the excel-based software ICPMSDataCal (Liu et al. 2008, 2010) and the results are summarized in Tables S10 and S11, respectively. Concordia diagrams and weighted mean calculations of U–Pb ages were made using Isoplot/Ex_ver4.15 (Ludwig 2003). εHf(t) values in this study are defined to denote the 1‰ difference between the sample and the chondritic reservoir (¹⁷⁶Hf/¹⁷⁷Hf = 0.282772, ¹⁷⁶Lu/¹⁷⁷Hf = 0.0384; Blichert-Toft and Albarede 1997) at the time of zircon growth.

Mineral chemistry

Garnet

Representative garnet grains were selected for major element mapping and quantitative profile analysis. Five zones (inner core, outer core, mantle, inner rim, outer rim) were identified for larger grains (Fig. 3a–d, i), whereas smaller grains only contain one to four of these five zones (Fig. 3e–i). Taking the larger grains as an example, the inner core (zone A) displays a patchy microstructure and has a composition (Alm_{40–44}Grs_{39–45}Prp_{13–16}Sps₁) that varies between different patches (Fig. 3a–d, i; Table S2). The other four zones are relatively homogeneous in composition.

The outer core (zone B; Alm_{35–40}Grs_{42–47}Prp_{15–18}Sps₁; Fig. 3; Table S2) contains the highest Ca and the lowest Fe contents among all the five zones. The mantle (zone C; Alm_{41–43}Grs_{35–39}Prp_{18–21}Sps₁; Table S2) and the inner rim (zone D; Alm_{49–51}Grs_{28–30}Prp_{19–21}Sps₁; Table S2) display a successive decrease of the Ca content and increase of the Mg and Fe contents (Fig. 3). There are three short transition zones between zone A, B, C, and D (Fig. 3i). A network of veinlets with strong BSE brightness occurs in the mantle (zone C) and inner rim (zone D) and ends at the core-mantle (zone A/B-zone C) interface (Fig. 3a, e). The veinlets are too thin for accurate measurements of their composition. In the outer rim (zone E), the contents of Ca, Fe, and Mn are slightly increased, which are compensated by a drop of the Mg content (Alm_{50–52}Grs_{28–31}Prp₁₈Sps₂; Fig. 3i; Table S2).

All the measured garnet zones (A, B, C, D; E is too thin to analyze) show a relatively flat distribution pattern of heavy rare earth elements (HREE; Lu_N/Dy_N = 1.06–1.36; Table S9) with weak Eu anomalies (δEu = 0.83–1.11; Fig. 4a; Table S9), but the trace element contents do vary between them. The contents of P, Ti, Na, and Ga increase from zone A to B and then decrease to zone C and D (Fig. 4b), whereas the contents of REE (such as Sm, Gd, Y, and Yb) vary in a reverse way (Fig. 4c). For transitional metal elements, (1) the content of Cr displays a gradual increase from zone A to zone D, (2) the contents of Co and Zn reach maxima in zone C, and (3) the content of V is similar between zone A and B and then decreases to C and D (Fig. 4d).

Other minerals

Omphacite in the matrix commonly shows a core-rim zoning. The core of matrix omphacite has a composition of Wo_{34–36}En_{30–31}Jd_{24–31}Ae_{0–6}Fs_{3–5}, while the rim of matrix omphacite has lower Na contents (Wo_{35–38}En_{29–35}Jd_{17–29}Ae_{0–13}Fs_{4–7}; Fig. S1a; Table S3). Diopside in the symplectite after omphacite displays a composition of Wo_{44–45}En_{35–37}Jd_{5–9}Ae_{2–4}Fs_{8–11} (Fig. S1a; Table S3). Phengite contains 3.2–3.6 Si, 1.81–2.42 Al, and 0.02–0.04 Ti per formula unit (p.f.u.), with the Si content decreasing towards the rim (Fig. S1b; Table S4). Biotite in the symplectite after phengite has a Ti content of 0.08–0.14 p.f.u. and a Mg* value (= Mg/(Mg + total Fe)) of 0.61–0.71 (Table S4). Amphibole contains a Si content of 6.12–6.86 p.f.u. and a Mg# (= Mg/(Mg + Fe²⁺)) value of 0.53–0.77 (Table S5). According to the classification scheme of Leake et al. (1997), amphibole in GJL10-8 is pargasite and edenite (Fig. S1c). Plagioclase in the symplectite after omphacite is generally albite (Ab_{68–97}An_{3–30}Or_{0–2}; Table S6), while that in the symplectite after phengite is richer in Ca (Ab_{64–73}An_{24–36}Or_{1–4}; Table S6). Clinzoisite has a X_{Fe} (= total Fe/(total Fe + Al)) value of 0.15–0.19 (Table S7). Dolomite and calcite display a composition of

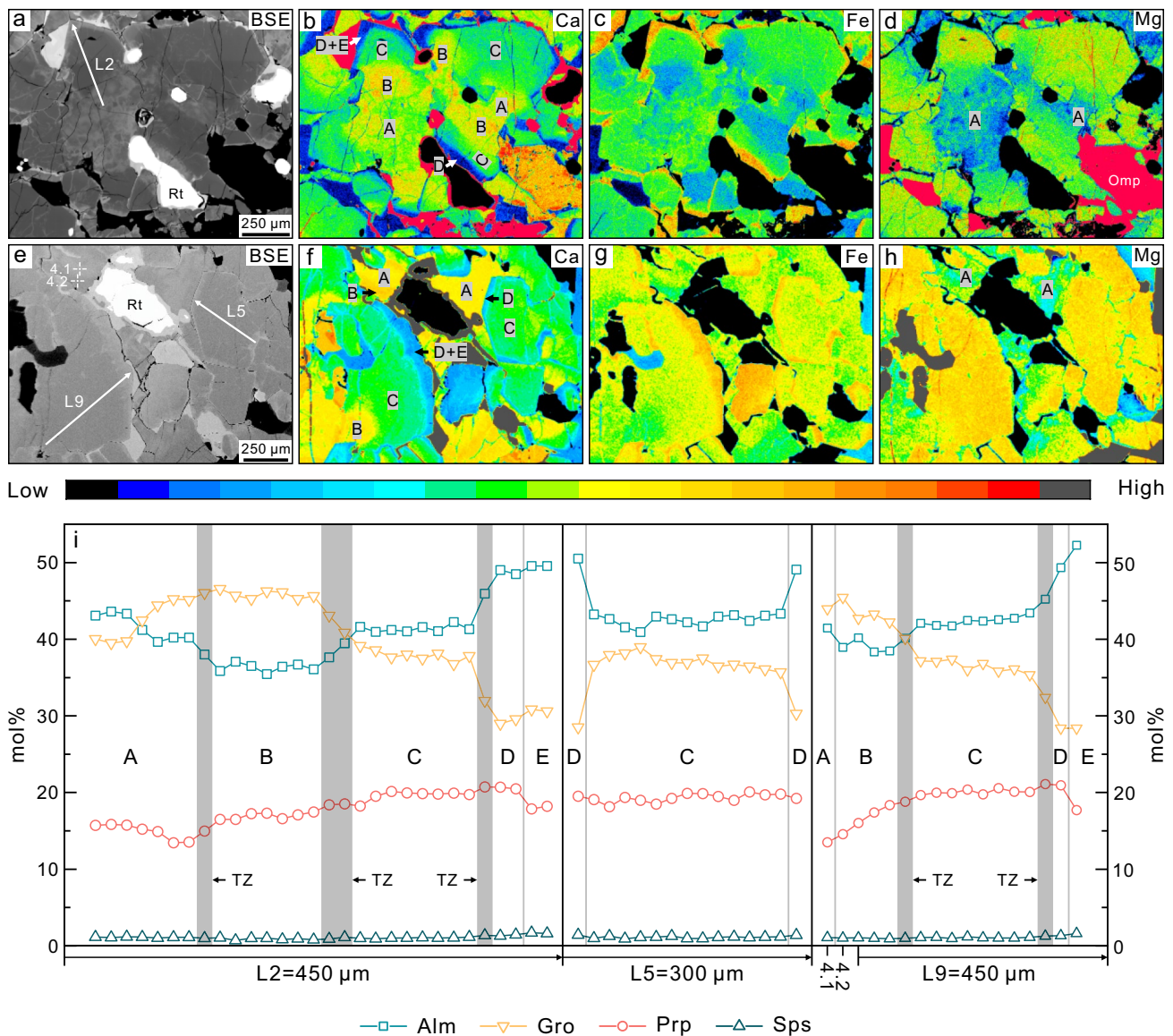


Fig. 3 Back-scattered electron (BSE) images (**a**, **e**), elemental concentration maps (**b–d** and **f–h**) and compositional profiles (**i**) of representative garnet grains in eclogite GJL10-8. **a–d** Larger garnet grains consist of a patchy inner core (zone A), an outer core (zone B with the highest Ca content), a discontinuous mantle (zone C with lower Ca content) and an inner rim (zone D with the lowest Ca content). An outer rim (zone E) can further be recognized in the compositional profile and contains a slightly higher Ca content than zone D. Note

that zone C and D are dissected by many microveins (**a**). **e–h** Smaller garnet grains contain one to four of the five zones defined for larger grains. Shaded regions in (**i**) are transitional zones (TZ) between adjacent zones. Two single spots (4.1 and 4.2) from another grain are plotted together with profile L9. See more details in main text. The locations of profiles and spot analyses are indicated in the BSE images. The color scale is adjusted to highlight the concentration variation in garnet and not identical for each map

$\text{Ca}_{50-51}\text{Mg}_{42-44}\text{Fe}_{6-8}(\text{CO}_3)_2$ and $\text{Ca}_{88-97}\text{Mg}_{1-7}\text{Fe}_{1-5}(\text{CO}_3)_2$, respectively (Table S8).

Zircon geochronology

Zircon in sample GJL10-8 is isometric or oval (aspect ratio of 1:1 to 1:2) with the long axis ranging from 60 to 130 μm (Fig. 5). CL imaging revealed a core-rim or a

core-mantle-rim zoning for many zircon grains. According to the CL feature, mineral inclusion distribution, and compositional variation, three main domains were identified for zircon.

Domain 1 commonly occurs in the core and is weakly zoned (Fig. 5a–e). It contains inclusions of coesite, garnet, omphacite, phengite, magnesite, dolomite, calcite, rutile, and apatite (Figs. 5a, b and 6; Table 1). Ten U–Pb analyses on domain 1 yielded concordant $^{206}\text{Pb}/^{238}\text{U}$ ages from

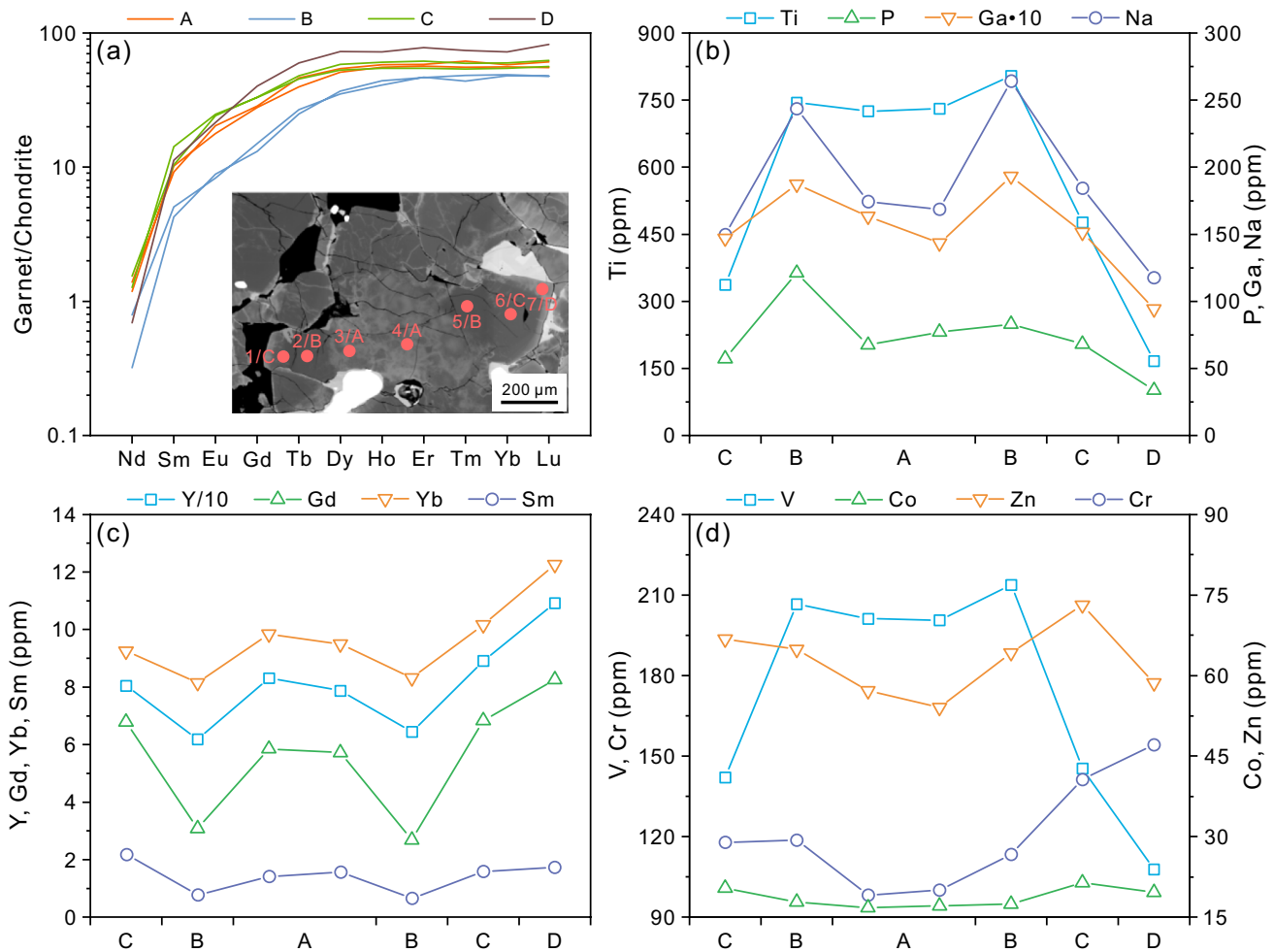


Fig. 4 Chondrite-normalized (after Sun and McDonough 1989) REE patterns (a) and trace element profiles (b–d) of different garnet zones in eclogite GJL10-8. Spot locations are shown in the inset image: the

number and letter next to the spot refers to the spot number and garnet zone, respectively

243 to 221 Ma, with a weighted mean age of 233 ± 6 Ma (MSWD = 6.7; Fig. 7a, b; Table S10). The Th content (12–54 ppm) of domain 1 is higher than the other two domains, but the U content (143–328 ppm) is relatively low (Fig. 8a; Table S10). The Th/U ratio (0.05–0.21) of domain 1 is normally greater than 0.1 (Fig. 8a; Table S10). Domain 1 shows a nearly flat HREE distribution pattern ($\text{Lu}_N/\text{Dy}_N = 1.50\text{--}2.41$) and weak Eu anomalies ($\delta\text{Eu} = 0.64\text{--}1.05$; Fig. 8b). This domain has a $\sum\text{MREEs}$ content of 5.1 to 23.0 ppm with a median of 13.0 ppm and an interquartile range (IQR) of 10.7–21.2 ppm (Fig. 8c; Table S10). The Ti contents of this domain have a range of 3.3–9.5 ppm, with a median of 5.9 and an IQR of 4.5–6.9 ppm (Fig. 8d; Table S10). Sixteen Lu–Hf analyses were conducted on domain 1, yielding a very low $^{176}\text{Lu}/^{177}\text{Hf}$ ratio of 0.000011–0.000027 (Table S11). The initial $^{176}\text{Hf}/^{177}\text{Hf}$ ratios (0.282563–0.282667) were calculated using the weighted mean age of domain 1 (233 Ma) and the decay

constant of ^{176}Lu of Söderlund et al. (2004), which are just the same as the measured $^{176}\text{Hf}/^{177}\text{Hf}$ ratios (Fig. 9a; Table S11).

Domain 2 shows a much weaker CL emission than domain 1 and 3. It is generally patchy zoned and occurs as mantles surrounding domain 1, or as cores where domain 1 is not present (Fig. 5e–g). Mineral inclusions are rare and only one garnet inclusion was identified in domain 2 (Table 1). Twenty U–Pb analyses on domain 2 yielded concordant $^{206}\text{Pb}/^{238}\text{U}$ ages from 243 to 226 Ma (Fig. 7; Table S10). The weighted mean age of domain 2 (232 ± 2 Ma, MSWD = 2.8) is the same as domain 1 within the uncertainties (Fig. 7b, c). Domain 2 contains a relatively low Th content (3.6–32.4 ppm) and a much higher U content (299–1185 ppm) than the other two domains, giving rise to a very low Th/U ratio (0.01–0.06; Fig. 8a; Table S10). The REE distribution pattern of domain 2 ($\text{Lu}_N/\text{Dy}_N = 1.05\text{--}3.00$; $\delta\text{Eu} = 0.58\text{--}1.17$) is similar to domain 1 (Fig. 8b; Table S10).

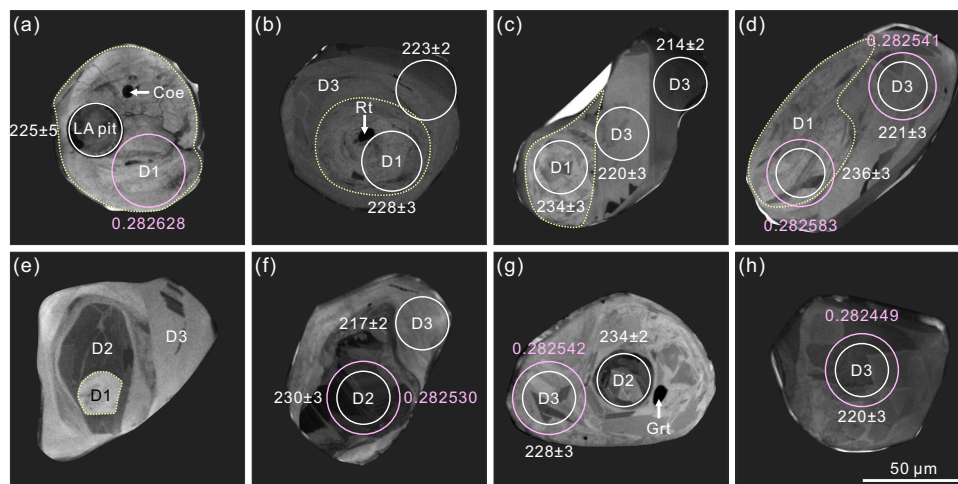


Fig. 5 Cathodoluminescence (CL) images of zircon in eclogite GJL10-8. Circles locate the sites of U–Pb analyses (white; $\varnothing=32\ \mu\text{m}$) and Lu–Hf analyses (pink; $\varnothing=44\ \mu\text{m}$), with corresponding $^{206}\text{Pb}/^{238}\text{U}$ ages ($\pm 1\sigma$; Ma) and $^{176}\text{Hf}/^{177}\text{Hf}$ values also shown. Three domains (D1, D2, D3) can be defined for the zircon. Domain

1 (outlined by yellow dashed lines) occurs as cores and is weakly zoned. Domain 2 is CL-dark and occurs as cores or mantles domain 1. Domain 3 is patchy zoned and mantles the other two domains or occurs as single grains. The scale in (h) applies to all the images. D1 Domain 1; D2 Domain2; D3 Domain3; LA Laser ablation

The ΣMREEs content of domain 2 is lower than domain 1 and varies from 3.3 to 21.2 ppm (one outlier of 49.5 ppm) with a median of 9.9 ppm and an IQR of 7.5–13.6 ppm (Fig. 8c; Table S10). Except for two outliers (14.5 and 13.7 ppm), domain 2 has a Ti content of 1.7–10.4 ppm with a median of 4.0 ppm and an IQR of 3.2–6.2 ppm (Fig. 8d; Table S10), slightly lower than the Ti content in domain 1. Fifteen Lu–Hf analyses on domain 2 yielded a $^{176}\text{Lu}/^{177}\text{Hf}$ ratio of 0.000004–0.000036 and an initial $^{176}\text{Hf}/^{177}\text{Hf}$ ratio (calculated at 232 Ma) of 0.282354–0.282607 (Fig. 9a; Table S11). While there is a slight overlap between the initial $^{176}\text{Hf}/^{177}\text{Hf}$ ratios of domain 1 and 2, domain 2 shows much lower values (Fig. 9a).

Domain 3 occurs as single grains or surrounds the other two domains. It displays a homogeneous or a patchy zoning and comprises 2 to 3 subdomains in some cases (Fig. 5b–h). Mineral inclusions identified in domain 3 include garnet, omphacite, quartz, calcite, rutile, and apatite (Figs. 5g and 6; Table 1). Twelve U–Pb analyses on domain 3 yielded concordant $^{206}\text{Pb}/^{238}\text{U}$ ages from 236 to 219 Ma, with a weighted mean age (222 ± 3 Ma; MSWD = 2.1) much younger than domain 1 and 2 (Fig. 7a, d; Table S10). Among the three domains, domain 3 contains the lowest Th (3.8–15.1 ppm) and U contents (171–351 ppm) and a Th/U ratio (0.02–0.06) comparable to that of domain 2 (Fig. 8a; Table S10). The REE distribution pattern of domain 3 ($\text{Lu}_N/\text{Dy}_N=1.63\text{--}3.42$; $\delta\text{Eu}=0.27\text{--}1.04$) is similar to the other two domains (Fig. 8b; Table S10). However, the ΣMREEs content of domain 3 (1.9–8.3 ppm; median = 4.8 ppm; IQR = 3.4–5.9 ppm) is much lower than the other two domains (Fig. 8b, c; Table S10).

Moreover, domain 3 contains a Ti content (4.3–15.8 ppm; median = 9.2 ppm; IQR = 7.4–11.0 ppm; Fig. 8d; Table S10) much higher than the other two domains. Twelve Lu–Hf analyses on domain 3 yielded a low $^{176}\text{Lu}/^{177}\text{Hf}$ ratio of 0.000009–0.000035 (Table S11). The initial $^{176}\text{Hf}/^{177}\text{Hf}$ ratios (0.282449–0.282636; calculated at 222 Ma) of domain 3 are in between those of domain 1 and 2 (Fig. 9a; Table S11).

Forward modeling and P–T estimates

Modeling methods

Forward modeling was performed using *Perple_X* (version 7.0.1, Connolly 2009) in the simplified system of Na–K–Ca–Fe–Mg–Mn–Al–Si–C–H–O. The thermodynamic dataset of Holland and Powell (2011) and the state equation of $\text{H}_2\text{O}\text{--CO}_2$ fluid of Holland and Powell (1991) were used. For solid and fluid solutions, the following models were selected: garnet, phengite, biotite and chlorite (White et al. 2014), omphacite (Green et al. 2007), amphibole (Green et al. 2016), feldspar (Fuhrman and Lindsley 1988), epidote (Holland and Powell 2011), magnesite and dolomite (Holland and Powell 1998), and fluid (Connolly and Trommsdorff 1991). Quartz, coesite, lawsonite, titanite, and rutile were treated as pure phases. As apatite is not considered in our calculation, the CaO in apatite was deducted from the measured bulk-rock composition. Using the Fe^{3+} contents in constituent minerals, 10–15% of the bulk-rock Fe was estimated to be Fe^{3+} (corresponding to additional O_2 content in the model system). A H_2O content (ca. 3 wt%) that can

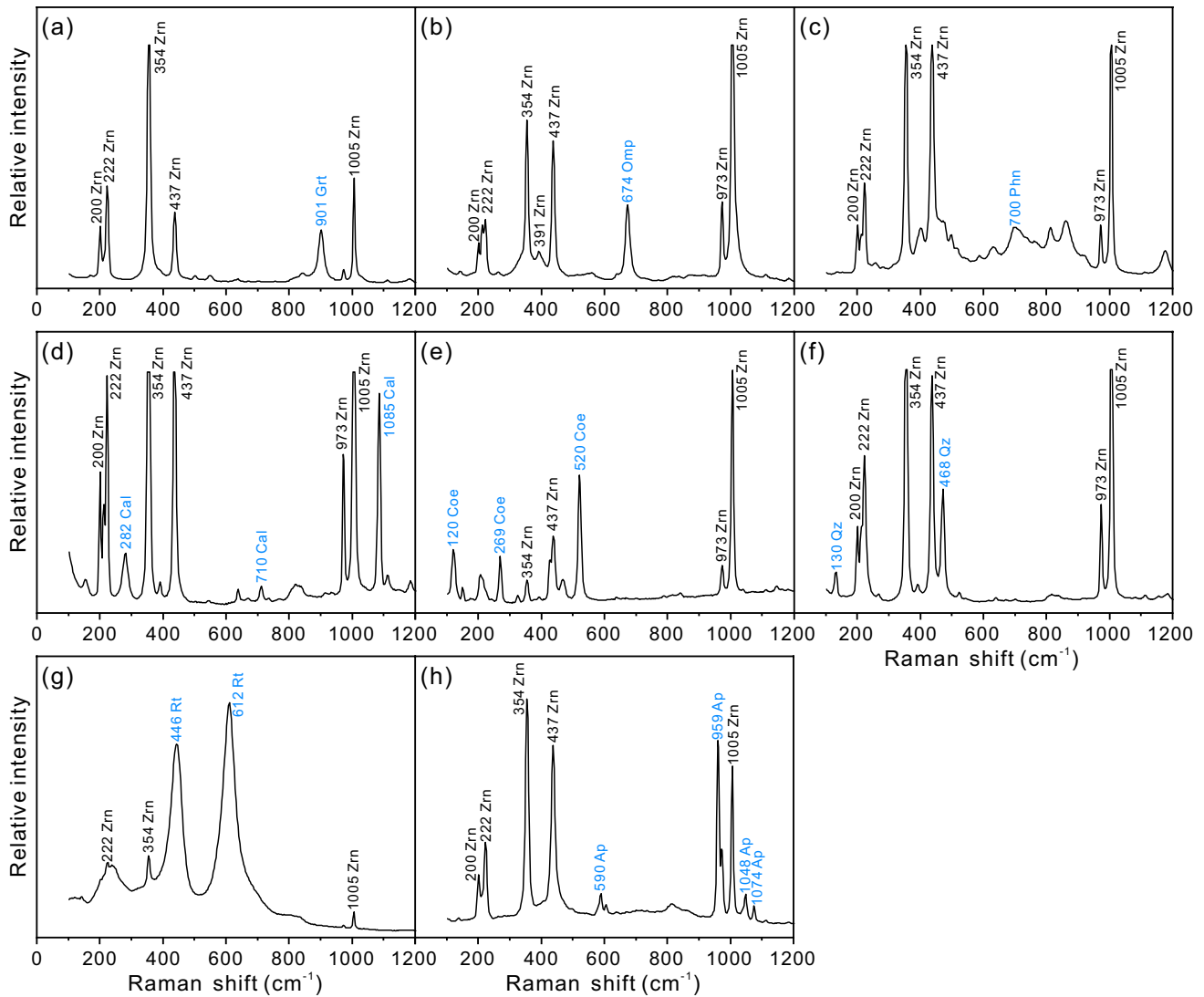


Fig. 6 Representative Raman spectra of mineral inclusions in zircon from eclogite GJL10-8: **a** garnet; **b** omphacite; **c** phengite; **d** calcite; **e** coesite; **f** quartz; **g** rutile; **h** apatite

Table 1 Statistic of mineral inclusions in different zircon domains from eclogite GJL10-8

Mineral	Grt	Omp	Phn	Coe	Qz	Mgs	Dol	Cal	Rt	Ap
Domain 1	43	52	2	5	1	1	1	3	44	15
Domain 2	1									
Domain 3	45	30			2			1	19	4

Inclusions were identified by laser micro Raman spectrometer and energy dispersive spectrometer

saturate the whole modeled P–T range with a fluid phase was used.

In order to constrain the P–T evolution, a P–T pseudosection was calculated in the P–T range of 1.0–5.0 GPa and 600–750 °C (Fig. 10). Noted is that the rock could have experienced a complicated carbonation and decarbonation history during metamorphism. Thus, it's hard to recover the bulk-rock CO₂ content for each metamorphic stage. The

carbonate content (ca. 3 vol%) in GJL10-8 indicates a bulk-rock CO₂ content of 1–1.5 wt% CO₂. However, a value of 2.5 wt% was chosen to calculate the P–T pseudosection. The major reason for this is to reproduce the highest grossular content measured in garnet in the modeled P–T range. To evaluate the influence of the CO₂ content on the modeling results, two T–X pseudosections at 3.5 and 4.5 GPa and

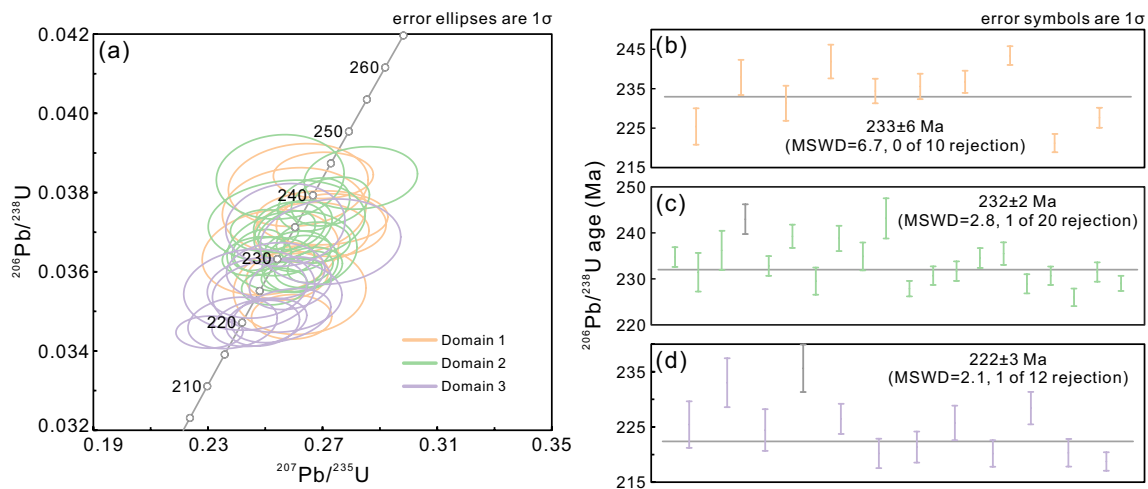


Fig. 7 **a** Concordia diagram showing the results of zircon U–Pb dating for eclogite GJL10-8. **b–d** Weighted mean $^{206}\text{Pb}/^{238}\text{U}$ ages calculated for individual zircon domains

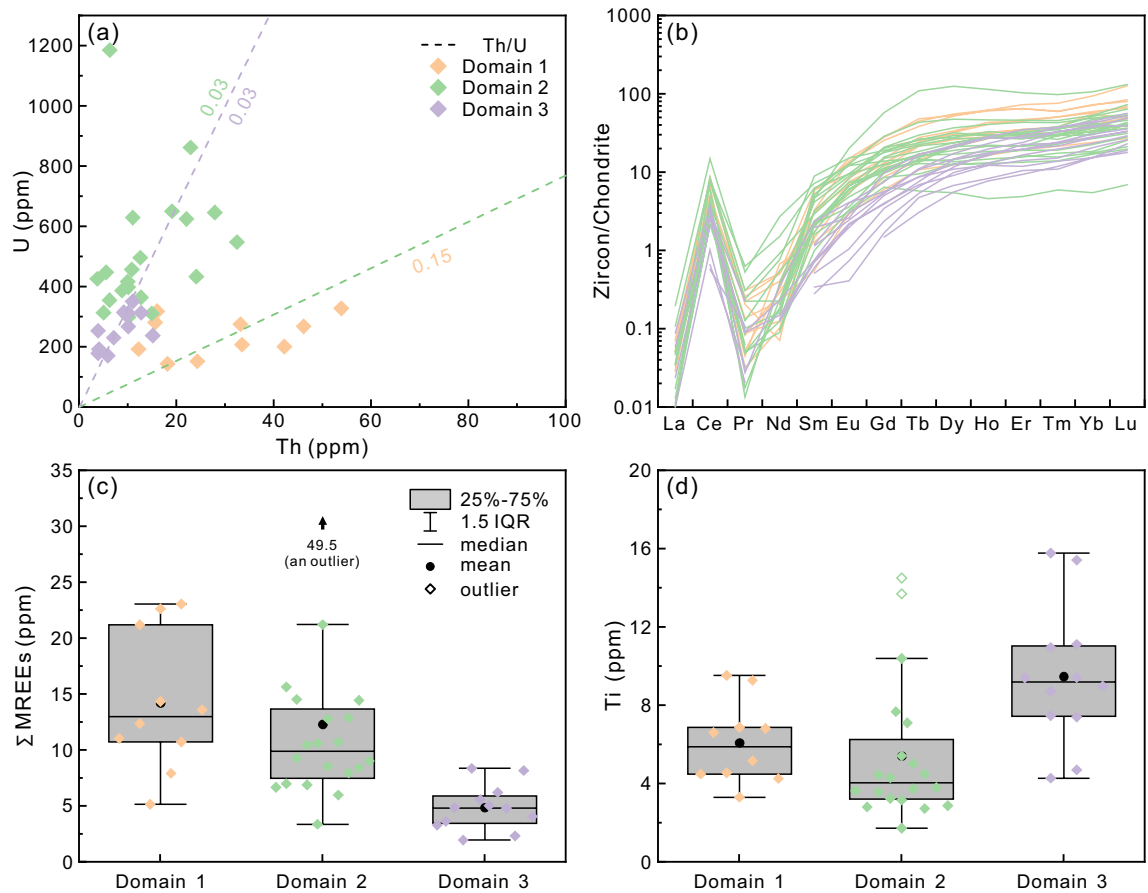


Fig. 8 Compositional diagrams of different zircon domains in eclogite GJL10-8. **a** U versus Th contents diagram. The dashed lines show the mean Th/U ratios of individual zircon domains. **b** Chondrite-normalized (after Sun and McDonough 1989) REE patterns. **c** Boxplot of ΣMREEs contents. **d** Boxplot of Ti contents. Parallel to the horizontal axis, single points in **c**, **d** are separated manually for clarity

malized (after Sun and McDonough 1989) REE patterns. **c** Boxplot of ΣMREEs contents. **d** Boxplot of Ti contents. Parallel to the horizontal axis, single points in **c**, **d** are separated manually for clarity

one P–X pseudosection at 700 °C were further calculated

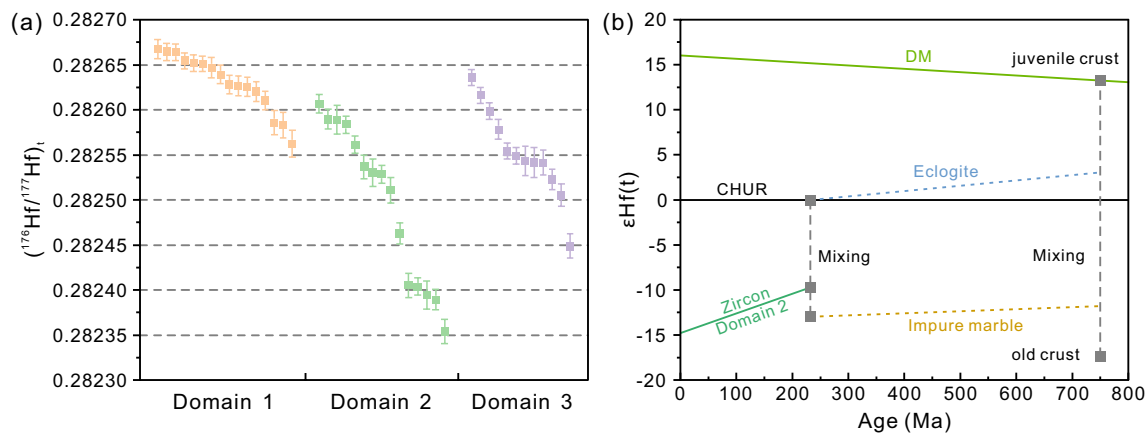


Fig. 9 **a** Distribution diagram of $(^{176}\text{Hf}/^{177}\text{Hf})_t$ of different zircon domains in eclogite GJL10-8. For clarity, single points are organized in descending order of their values. **b** Diagram showing the evolution of zircon $\epsilon\text{Hf}(t)$. The evolution line of depleted mantle (DM) was

derived from $\epsilon\text{Hf}(t)=16$ at present (average mid-ocean ridge basalt value; Nowell et al. 1998) and $\epsilon\text{Hf}(t)=6$ at 2.7 Ga (Vervoort et al. 1999). The evolution lines of eclogite and impure marble are schematic. CHUR chondritic uniform reservoir

(Fig. 11). The effective bulk-rock compositions (EBCs) used for modeling are shown in Table S1.

Modeling results

Petrographic features and mineral inclusions in zircon suggest a peak UHP mineral assemblage of garnet + omphacite + phengite + coesite + magnesite \pm dolomite + rutile for the eclogite (Table 1). According to the modeling results, this assemblage is stable at pressures higher than 3.5 GPa at 700 °C (Fig. 10a). Phengite in GJL10-8 contains a Si content up to 3.6 p.f.u. (Table S4), which indicates a minimum peak pressure of 4.0 GPa at 700 °C (Fig. 10c). The composition of garnet zone A falls in the lawsonite field at UHP conditions: (1) some Mg-rich patches contains 39–40 mol% grossular and 16 mol% pyrope (Fig. 3i), the isopleths of which intersect at 3.2–3.4 GPa and 620–630 °C in the field of garnet + omphacite + phengite + lawsonite + coesite + magnesite + dolomite + rutile (Fig. 10a); and (2) the other compositional patches (42–45 mol% grossular and 13–15 mol% pyrope; Fig. 3i) yielded low-angle intersections in the field of garnet + omphacite + phengite + lawsonite + coesite + magnesite + rutile and no conclusive P–T intersections can be obtained (Fig. 10a, d, e). Garnet zone B contains 45–47 mol% grossular and 16–17 mol% pyrope (Fig. 3i), which indicate higher P–T conditions than zone A and are suggested to represent the peak composition (Fig. 10d, e). The compositional isopleths of zone B are nearly parallel to each other in the UHP field, but its grossular contents suggest a peak P–T condition higher than 3.9–4.6 GPa and 680–750 °C (Fig. 10d). Garnet zone C and D contain successively lower grossular and higher pyrope contents and this compositional variation trend reverses in zone E (Fig. 3i). As discussed later, these

three zones resulted from a dissolution and reprecipitation process and the EBCs responsible for their formation cannot be estimated. Nevertheless, the modeling results shown in Fig. 10 can still be used to constrain relevant P–T evolution in a semiquantitative way. To do so, the magnitudes of compositional variations between garnet zones were especially considered. This finally yielded a nearly isothermal decompression P–T path (Fig. 10d, e). Along this P–T path, the grossular content decreases and the pyrope content increases quickly in the field of garnet + omphacite + phengite + coesite + magnesite + dolomite + rutile, which most likely corresponds to the formation stage of zone C. In the same way, zone D is interpreted to have formed in the field of garnet + omphacite + phengite + epidote + quartz \pm dolomite + rutile. The growth of dolomite by consuming magnesite and epidote by consuming garnet should have determined the compositional changes from zone B to C and then to D, respectively (Fig. 10b). With further decompression, the amphibole formation could lead to the increase of grossular content and the decrease of pyrope content in garnet zone E (Fig. 10b).

The minimum peak P–T conditions inferred from the peak mineral assemblage and the Si content in phengite change little with the bulk-rock CO_2 content in the range of 1–5 wt% (Fig. 11a, b). Neither changes the general shape of the decompression P–T path (Fig. 11c, d). In contrast, the P–T conditions recorded by garnet zone A and B do change. With more CO_2 in the bulk-rock, the field of garnet + omphacite + phengite + lawsonite + coesite + magnesite + dolomite + rutile gets extended to lower temperatures and higher pressures and to accommodate more compositional intersections of garnet zone A (Fig. 11a–c). In addition, the modeled maximum grossular content increases with the bulk-rock CO_2 content: the usage of

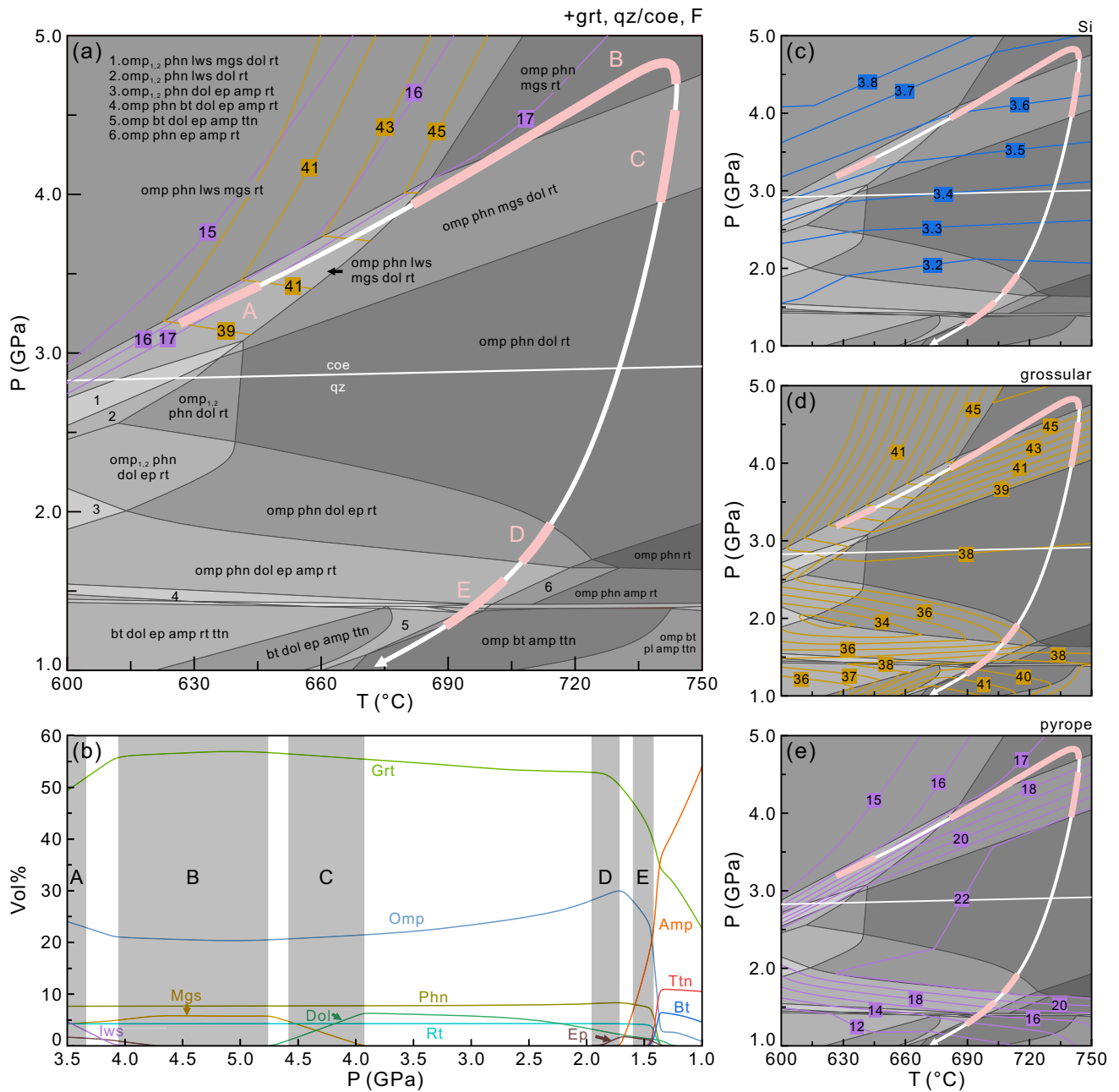


Fig. 10 Contoured P–T pseudosections calculated for eclogite GJL10-8 in the system Na–K–Ca–Fe–Mg–Mn–Al–Si–C–H–O with the effective bulk-rock composition (EBC) in Table S1. **a** P–T pseudosection with darker shaded fields indicating higher variances. Some fields are not labelled for the sake of clarity. **b** A diagram showing the changes of mineral volume contents in GJL10-8 along a linear P–T

path from 3.5 GPa and 645 °C to 5.0 GPa and 750 °C and then to 1.0 GPa and 675 °C. **c** Isoleths of Si content (p.f.u.) in phengite. **d, e** Isoleths of grossular and pyrope contents (mol%) in garnet, respectively. The bold arrow line is the P–T path reconstructed in this study. A, B, C, D, and E on the P–T path indicate the formation stages of different garnet zones. See more details in main text

a value less than 2.5 wt% cannot reproduce the highest grossular content measured in zone B in the modeled P–T range, while a value between 2.5 and 5.0 wt% does not change the minimum P–T conditions recorded by zone B (Fig. 11b–d). Even with these P–T uncertainties, a general clockwise P–T path as shown in Fig. 10 can still be

outlined: (1) garnet zone A records a prograde P–T condition in the field of garnet + omphacite + phengite + lawsonite + coesite + magnesite ± dolomite + rutile; (2) garnet zone B records a peak P–T condition in the field of garnet + omphacite + phengite + coesite + magnesite ± dolomite + rutile; (3) garnet zone C, D, and E record a nearly

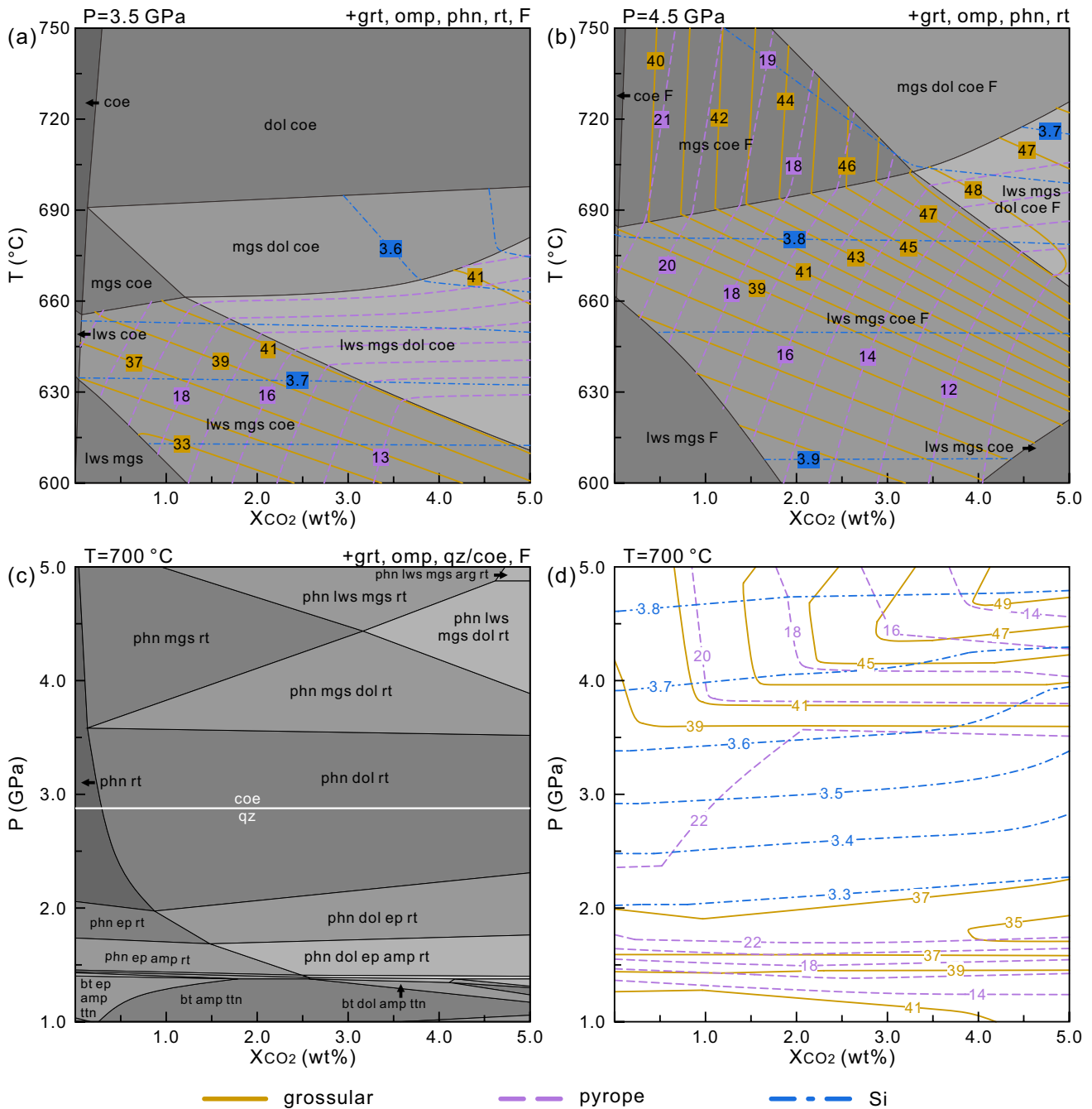


Fig. 11 Contoured P/T-X_{CO₂} (wt% in bulk rock) pseudosections calculated for eclogite GJL10-8 in the system Na-K-Ca-Fe-Mg-Mn-Al-Si-C-H-O with bulk-rock compositions X1 and X2 in Table S1. **a, b** Contoured T-X_{CO₂} pseudosection at 3.5 GPa and 4.5 GPa,

respectively. **c, d** Contoured P-X_{CO₂} pseudosection at 700 °C. Isopleths of Si content (p.f.u.) in phengite and grossular and pyrope contents (mol%) in garnet are plotted for each pseudosection

isothermal decompression still within eclogite-facies; and (4) the symplectites after omphacite and phengite record a typical amphibolite-facies retrogression. In Fig. 12 and Table 2 is summarized the evolution history of eclogite GJL10-8.

P-T estimates from Ti-in-zircon thermometer

The P-dependent Ti-in-zircon thermometer newly calibrated by Crisp et al. (2023) was applied and the TiO₂ and SiO₂ activities were both assumed as one given the occurrence of

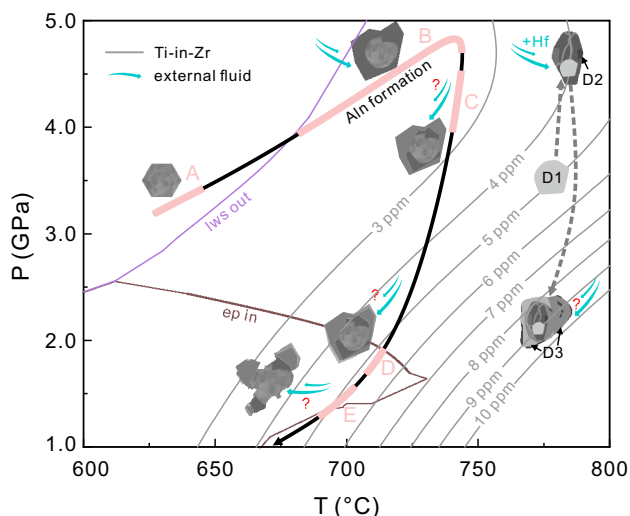


Fig. 12 Schematic diagram that outlines the multistage formation of garnet and zircon in eclogite GJL10-8. The isopleths of Ti contents in zircon calculated from the calibration of Crisp et al. (2023) are plotted. The P–T path recorded by zircon deviates from the P–T path recorded by garnet to a hotter regime, which can be partly attributed to the analytical uncertainties of Ti in zircon. Whether the fluids active during decompression were externally derived is ambiguous and indicated by question marks. See discussion in the main text

rutile and coesite/quartz in GJL10-8. The analytical uncertainties (1σ) of Ti contents in zircon were in the range of 15–20% in our study, which would be propagated to the calculated temperatures.

Domain 1 of zircon in GJL10-8 includes coesite, dolomite, and magnesite (Table 1) and is interpreted to have formed at a UHP stage (Fig. 10a). Domain 2 contains a Ti content slightly lower than domain 1 (Fig. 8d) but texturally later (Fig. 5e). According to their similar ages (Fig. 7) and the distribution of Ti-in-zircon isopleths in P–T space (Fig. 12), it is inferred that domain 1 and 2 most likely formed shortly before and at the peak UHP stage, respectively. Domain 1 records a crystallization temperature of 739–847 (median = 795; IQR = 768–812) °C at 3.5 GPa, while domain 2 records a crystallization temperature of 705–891 (median = 785; IQR = 762–831) °C at 4.5 GPa. Domain 3 most likely formed in the stability field of epidote during early exhumation (see discussion part) and records a crystallization temperature of 701–827 (median = 771; IQR = 750–789) °C at 2.0 GPa.

Discussion

Zoned garnet as a witness of P–T changes and pervasive fluid–rock interactions: the key role of dissolution and reprecipitation

Evidence on the prograde history before UHP peak has been rarely documented for the Dabie–Sulu UHP rocks (Ebanu and Nagasaki 1999; Taguchi et al. 2016; Zhang et al. 2005). It has been proposed that the Dabie–Sulu UHP eclogites could have evolved through the stability field of lawsonite

Table 2 Metamorphic evolution of eclogite GJL10-8

Stage	I	II	III	IV	V
Note	Prograde	Peak UHP	UHP-EG	HP-EG	AM
Grt	Grt_A	Grt_B	Grt_C	Grt_D&E	
Cpx	Omp				Di
Phn		Si \geq 3.6 p.f.u.			
Bt					
Coe					
Qz					
Lws					
Aln					
Ep					
Amp					
Pl					
Mgs					
Dol					
Cal					
Rt					
Ttn					

EG Eclogite facies; AM Amphibolite facies

EG Eclogite facies; AM Amphibolite facies

during prograde metamorphism (Guo et al. 2012, 2013; Li et al. 2004; Wei et al. 2013). Garnet zone A in this study acts as a piece of potential evidence on this prograde metamorphism (Fig. 10a). It is noteworthy that garnet zone A shows a patchy microstructure (Fig. 3a), a typical alteration result from dissolution and reprecipitation (Faryad et al. 2018; Konrad-Schmolke et al. 2007; Kulhánek et al. 2021; Putnis 2002; Vho et al. 2020). The fluid responsible for this alteration could have been sourced either from the prograde breakdown of lawsonite or from an external source (see later discussion). Garnet zone A is connected to zone D and E by a network of veinlets in zone C (Fig. 3a). The veinlets are interpreted as microfractures that have been healed and formed later than zone C. Earlier studies suggested that these microfractures could behave as efficient channels for fluids to alter the garnet interiors (Bovay et al. 2021; Giuntoli et al. 2018; Vho et al. 2020). This indicates that the patchy microstructure observed in this study could have alternatively formed at a retrograde stage, for example, at the same time with garnet zone D or E. Nevertheless, garnet zone A shows very different compositions to zone D or E (Fig. 3i), thus, ruling out this possibility.

Garnet zone B contains the highest grossular contents among all the garnet zones and is interpreted as a peak growth after zone A (Figs. 3i and 10d). This explanation is supported by the highest contents of P, Ti, and Na measured in zone B (Fig. 4b) since these minor elements can be positively correlated with pressure (Hermann and Spandler 2008; Konzett and Frost 2009). This garnet zone records a minimum peak P–T condition of 3.9–4.6 GPa and 680–750 °C (Fig. 10a, d), comparable to earlier estimates for the Dabie UHP rocks (Liu et al. 2015, 2019; Schmid et al. 2000; Wei et al. 2013). The highest grossular contents in garnet zone B are mainly attributed to the final breakdown of lawsonite during prograde metamorphism (Fig. 10a). As discussed later, a Ca-bearing C–H–O fluid from the host marble could have infiltrated the eclogite at the peak stage. There is no wonder that the addition of Ca could have increased the grossular content in garnet zone B. Moreover, the addition of CO₂ has to be considered since the peak garnet composition may change with the bulk-rock CO₂ content: (1) if garnet zone B had formed in the field of garnet + omphacite + phengite + lawsonite + coesite + magnesite + dolomite + rutile, the influence could have been minor; (2) if garnet zone B had formed in the field of garnet + omphacite + phengite + lawsonite + coesite + magnesite + rutile, the addition of CO₂ could have contributed to the increase of its grossular content (Fig. 11). It should be noted that garnet zone B also contains higher pyrope contents than zone A (Fig. 3i). This cannot be interpreted only by infiltration of an Ca-bearing C–H–O fluid. Otherwise, the pyrope content would have decreased in garnet zone B (Fig. 11b–d). Therefore, lawsonite breakdown related to P–T

changes should have dominated over the infiltration of an Ca-bearing C–H–O fluid in shaping the major element composition of garnet zone B.

Garnet zone C, D, and E record a nearly isothermal decompression P–T path, along which the modal content of garnet would decrease (Fig. 10b). Thus, these three garnet zones are interpreted to have formed from re-equilibration of former garnet instead of as new growth zones. Compositional re-equilibration of garnet depends on two basic mechanisms, i.e. diffusion and dissolution-reprecipitation (Kohn 2014; and references therein). Elemental exchange with other minerals by diffusion generally forms a transitional zoning in garnet, which contradicts with the relatively flat compositional profiles observed for each of the three retrograde garnet zones (Fig. 3i). In contrast, dissolution-reprecipitation generally forms a sharp zoning boundary that is shared by different elements (Cheng et al. 2007; Giuntoli et al. 2018; Martin et al. 2011). The compositional contacts between different garnet zones in this study are largely stepwise (Fig. 3i) and more compatible with a dissolution-reprecipitation mechanism. The short transitional zones between different zones can be attributed to modifications of following interface diffusion. Depending on the precipitated sites of dissolved materials, dissolution and reprecipitation can be space-coupled (i.e. pseudomorphic) or -uncoupled at the submicroscopic scale (Giuntoli et al. 2018; Martin et al. 2011). In this study, space-coupled dissolution and reprecipitation is preferred for larger garnet grains because most of them retained their intact shape after the formation of garnet zone C, D, and E (Fig. 3a, e), which is a typical space-coupled result (Martin et al. 2011; Putnis and Mezger 2004; Smit et al. 2008). Space-uncoupled dissolution and reprecipitation must have also taken place as some smaller grains among garnet aggregates display corroded outlines (Fig. 3e).

Since dissolution-reprecipitation needs the action of fluids, the repeated actions of such a mechanism in altering garnet composition suggest multistage fluid–rock interactions during exhumation. Moreover, the alteration patterns of garnet and the formation of healed fractures in garnet (Fig. 3) indicate fluid flow along grain boundaries and microfractures, i.e., the fluid–rock interactions were pervasive (Ague 2014). The fluids responsible for the garnet compositional alteration during exhumation could have been either externally or internally derived. In the case of an external origin, more Ca-bearing C–H–O fluids could have infiltrated the eclogite during exhumation (Fig. 12). The addition of Ca could increase the grossular contents in garnet, which is consistent with the compositional recordings of garnet zone E but not with those of zone C and D (Fig. 3i). Meanwhile, the addition of CO₂ had little influence on the garnet composition (Fig. 11d). Again, it can be concluded that P–T changes instead of infiltrated Ca-bearing C–H–O fluids have

dominated the compositional changes of major elements in garnet zone C, D, and E.

It is noteworthy that the REE contents in garnet first decrease from zone A to zone B and then increase to zone C and D (Fig. 4c). Garnet is the major host of HREE in eclogite (Liu et al. 2019; Spandler and Pirard 2013). The decrease and increase of the HREE contents can get explained by the prograde growth and retrograde breakdown of garnet, respectively (Fig. 10b). The decrease of LREE and MREE contents in garnet zone B could have been related to the breakdown of lawsonite and the formation of allanite at the peak stage (Fig. 12), the latter of which can sequester considerable LREE and MREE from the bulk rock (Martin et al. 2014; also see later discussion). It's more complicated to explain the increase of LREE and MREE contents in garnet zone C and D. The breakdown of garnet could have also released some MREE but not LREE during exhumation. Infiltration of external fluids could have introduced extra LREE and MREE into the eclogite.

Multiple generations of eclogite-facies zircons: the compositional influences of epidote-group minerals and pressure decrease

All the three zircon domains display a flat HREE distribution pattern and weak Eu anomalies (Fig. 8b) and contain eclogite-facies mineral inclusions (Table 1), suggesting that they formed at eclogite-facies conditions (Rubatto 2002; Whitehouse and Platt 2003). Without anatexis, metamorphic zircon can form from the following mechanisms: solid-state and fluid-aided recrystallization of former magmatic zircons and growth from fluids (e.g. Geisler et al. 2007; Hoskin and Black 2000; Rubatto and Hermann 2003). Solid-state recrystallization is inefficient in resetting the composition of former magmatic zircons (Chen et al. 2010; Hoskin and Black 2000) and thus cannot explain the concordant U–Pb ages or the REE features of the studied zircon. The other two mechanisms are largely equivalents to the space-coupled and -uncoupled dissolution-reprecipitation discussed above. They can guarantee the concordance of U–Pb ages and equilibration of trace element composition of metamorphic zircon with surrounding minerals (Chen et al. 2010; Harlov et al. 2023; Martin et al. 2008) and are preferred to explain the formation of the studied zircon. Consequently, the eclogite-facies zircons provide another evidence for multistage pervasive fluid–rock interactions that had happened in the eclogite.

Metamorphic zircons commonly have a Th/U ratio below 0.1 (Rubatto 2017; and references therein), but zircon domain 1 in this study has a Th/U ratio higher than 0.1 (Fig. 8a). One can argue that the high Th/U could have inherited from former magmatic zircons after recrystallization. If so, the REE pattern must have also inherited the magmatic

left-declined feature to some extents (Chen et al. 2010). However, this is not the case. A closer examination reveals that the high Th/U in zircon domain 1 is mainly related to its high Th contents (Fig. 8a). The presence of allanite and monazite (two Th-rich phases) has been invoked as a reason for low Th/U in coexisting metamorphic zircon (Rubatto et al. 2009; Stepanov et al. 2016; Yakymchuk et al. 2018). As presented above, zircon domain 1 formed at a prograde UHP stage, likely in the stability field of lawsonite (Fig. 12). The absence of allanite and monazite could have produced metamorphic zircon with high Th contents and high Th/U at this stage. Prograde lawsonite breakdown would release LREE and Th (Martin et al. 2014) so to facilitate the formation of allanite at the peak stage. Allanite has a wide stability field in P–T space (Hermann 2002; Poli and Schmidt 2004) and occurs in the eclogite (Fig. 2e). The formation of allanite after lawsonite can explain the low Th/U in zircon domain 2 and 3 (Fig. 8a). It is noteworthy that zircon domain 2 also contains higher U contents than the other two domains. As discussed below, an external fluid infiltrated the eclogite during the formation of zircon domain 2. Uranium (in the state of U^{6+}) is more soluble than Th in aqueous fluids (Kessel et al. 2005; Spandler et al. 2007). The introduction of U by external fluids could have contributed to the higher U contents in zircon domain 2.

Zircon domain 2 contains slightly lower \sum MREEs contents than domain 1, while the \sum MREEs contents become further lower in domain 3 (Fig. 8b, c). These compositional variations can be best interpreted by the formation of MREE-rich minerals in the eclogite. Zircon domain 2 most likely formed at the peak stage and coexisted with allanite (see above). Compared to lawsonite, allanite is not only richer in LREE but also richer in MREE (Martin et al. 2014). Thus, the formation of allanite after lawsonite can explain the slight decrease of \sum MREEs contents in zircon domain 2. During exhumation, more and more epidote formed in the eclogite at pressures below 2.0–2.5 GPa (Fig. 10a). Epidote is also a LREE- and MREE-rich mineral although not so rich as allanite (El Korh et al. 2009; Hermann 2002; Spandler et al. 2003). The further decrease of \sum MREEs contents in zircon domain 3 can be interpreted by the gradual formation of retrograde epidote. In fact, zircon domain 3 also contains lower \sum LREEs contents than domain 1 and 2 (Fig. 8b), which is another indicator of epidote coexistence. However, the LREE contents in zircon domain 3 are often below the detection limits so that a quantitative comparison cannot be made. In addition to epidote, the retrograde growth of titanite and amphibole may have also exerted an influence on the MREE contents in zircon domain 3 (El Korh et al. 2009; Sassi et al. 2000; Spandler et al. 2003). However, titanite and amphibole mainly formed at the amphibolite-facies stage and do not occur as inclusions in zircon domain 3. Thus, their influence can be neglected.

Zircon domain 3 contains higher Ti contents than domain 1 and 2 (Fig. 8d). In general, higher Ti contents in zircon are interpreted to reflect higher temperatures (e.g. Chen et al. 2013; Gao et al. 2011; Stepanov et al. 2016). However, pressure also exerts a control on the Ti incorporation in zircon (Ferriss et al. 2008; Tailby et al. 2011). The influence of pressure has to be considered especially for UHP rocks that traveled through a large pressure window. As discussed above, zircon domain 3 formed during exhumation. According to the distribution of Ti-in-zircon isopleths in P–T space, a nearly isothermal decompression P–T path as reconstructed in this study could also lead to the increase of Ti contents in zircon (Fig. 12). Different zircon domains record temperatures higher than 750 °C with the highest values more than 800 °C (Fig. 12). Such high temperatures are somewhat inconsistent with the preservation of the stepwise zoning pattern of garnet since fast volume diffusion at high temperatures could have erased this zoning pattern (Caddick et al. 2010; Carlson 2006; Ganguly et al. 1998). Besides, if the temperatures recorded by zircon were realistic, extensive hydrous melting should have occurred but were not observed in the eclogite. Since the Ti-in-zircon thermometer may have overestimated the metamorphic temperatures, we tentatively limit the peak temperature below 750 °C (Fig. 12) by referring to our early studies on the Ganjialing area (Liu et al. 2015, 2019).

In view of the above discussion, we can assume that zircon domain 2 and 3 formed at 4.5 and 2.0 GPa, respectively. The mean age difference between these two domains is 10 ± 5 Ma. Using these parameters, the early exhumation rate was roughly estimated. The result is 5.5–16.5 mm/y, with the upper limit higher than earlier estimates for the Dabie–Sulu UHP rocks (5.0–11.3 mm/y; Liu and Liou 2011; and references therein). It corresponds to a low to intermediate exhumation rate among all the (U)HP terranes (Hermann and Rubatto 2014).

Zircon Hf isotopes: insights into external fluids influx and Hf mobility

Zircon domain 2 formed later and contains much lower $(^{176}\text{Hf}/^{177}\text{Hf})_t$ than domain 1 (Fig. 9a). Zircon is the major host for Hf and has the lowest Lu/Hf (< 0.0001) among common metamorphic minerals (Rubatto 2017; Spandler and Pirard 2013). Re-equilibration with other minerals normally elevates $^{176}\text{Hf}/^{177}\text{Hf}$ in zircon in a closed rock system (Zheng et al. 2005b). Taking lawsonite and epidote as two examples, both minerals contain much higher Lu/Hf than zircon, breakdown or dissolution of the two minerals would lead to a higher $^{176}\text{Hf}/^{177}\text{Hf}$ in growing zircon. Thus, the lower $(^{176}\text{Hf}/^{177}\text{Hf})_t$ in zircon domain 2 most likely reflects an infiltration of external fluids. The Hf isotopic composition of zircon domain 2 is more heterogeneous than domain 1, supporting that domain 2

had been in disequilibrium with an infiltrated fluid. It should be noted that the protolith of marble-hosted eclogites in the Dabie–Sulu UHP terrane is marl and/or basaltic tuff (Chen et al. 2016; Wu et al. 2006) and could have contained detrital materials with various origins. In such a case, another possibility must be evaluated. Considering that zircon is the major host of Hf in most rocks (Spandler and Pirard 2013; and references therein), the compositional difference of Hf isotopes between zircon domains 1 and 2 might be an inherit of two groups of detrital zircons. Such a selective inherit seems highly unlikely in the presence of fluids as there is no reason why low $^{176}\text{Hf}/^{177}\text{Hf}$ detrital zircon did not participated the formation of zircon domain 1 at the very beginning. The $(^{176}\text{Hf}/^{177}\text{Hf})_t$ of zircon domain 3 is in between those of domain 1 and 2. It is ambiguous if this is a just inherit of the earlier two domains or had involved any infiltrated fluids (Fig. 12). Compared to zircon domain 2, domain 3 shows higher $(^{176}\text{Hf}/^{177}\text{Hf})_t$, which can be partly attributed to the incorporation of radiogenic Hf released by garnet during HP recrystallization.

The $\epsilon\text{Hf}(t)$ of zircon domain 2 is -9.70 to -0.76 at the crystallization time, much lower than that of domain 1 (-2.31 to 1.40 ; Table S11). The negative $\epsilon\text{Hf}(t)$ of zircon domain 2 suggests that the infiltrated fluid originated from an evolved crustal reservoir, such as the host marble (Fig. 9b). More importantly, the significant decrease of $^{176}\text{Hf}/^{177}\text{Hf}$ in zircon domain 2 indicates that Hf can be efficiently mobilized by fluids at UHP conditions. As an important HFSE, Hf is insoluble in aqueous fluids (Ayers and Watson 1991; Kovalenko and Ryzhenko 2009; Schmidt et al. 2006). However, experimental studies have demonstrated that the presence of Na–Al–silicate and CaCl_2 components can boost the dissolution of Zr in aqueous fluids by forming alkali zircon-silicate and $\text{Ca}_3[\text{Zr}(\text{OH})_6]^{4+}$ complexes, respectively (Brendebach et al. 2007; Wilke et al. 2012). Hafnium behaves geochemically similar with Zr due to their similar ionic radii and charges (Hf^{4+} vs. Zr^{4+}). Thus, it is inferred that Hf can be also mobilized by similar complexes. The infiltrated fluid is explained to have originated from the host impure marble in this study, which must have been a CO_2 -bearing aqueous fluid (Castelli et al. 2007; Liu et al. 2015). The role of CO_2 component in influencing the mobility of Hf is unclear now and calls for attention in the future. Meanwhile, recent forward modeling and fluid inclusion studies demonstrated that UHP C–H–O fluids in impure marbles could dissolve considerable Ca (Connolly and Galvez 2018; Maffei et al. 2021). This provides a feasible geochemical context for Hf mobilization.

Conclusions

Garnet and zircon in a marble-hosted eclogite from the Dabie UHP terrane show complex zoning patterns and document multistage pervasive fluid–rock interactions during

deep subduction and exhumation. The inner patchy and outer cores of garnet likely record a prograde breakdown of lawsonite to UHP peak (3.0–4.5 GPa and 630–750 °C) and their formation could have also involved a Ca-metasomatism. The mantle and inner and outer rims mainly resulted from dissolution and reprecipitation of former garnet and record a nearly isothermal decompression at eclogite-facies conditions. Zircon domain 1 (243–221 Ma; mean = 233 ± 6 Ma) formed at a prograde UHP stage and likely in the stability field of lawsonite. The relatively high Th/U is related to the absence of allanite during its formation. Zircon domain 2 (243–226 Ma; mean = 232 ± 2 Ma) formed at the UHP peak. The lower $^{176}\text{Hf}/^{177}\text{Hf}$ in this domain suggests that an external Ca-bearing C–H–O fluid from the host marble introduced Hf into the eclogite. Zircon domain 3 (236–219 Ma; mean = 222 ± 3 Ma) formed at early exhumation and contains much higher Ti and lower ΣMREEs contents than the other two domains, which reflect pressure decrease and epidote formation, respectively. The early exhumation rate was estimated to be in the range of 5.5–16.5 mm/y, corresponding to a low to intermediate exhumation rate among all the (U)HP terranes.

Supplementary Information The online version contains supplementary material available at <https://doi.org/10.1007/s00410-024-02158-5>.

Acknowledgements This study was funded by the National Natural Science Foundation of China (Grant No. 92058208) and the National Key Research and Development Project of China (Grant No. 2023YFF0804101). Wu Y.B. (Wuhan) and Chen R.X. (Hefei) provided insightful discussions. The authors also acknowledge the constructive comments from editor Daniela Rubatto, Zeb Page and an anonymous reviewer, which improved the manuscript.

Data availability All the used data have been provided as supplementary materials in this paper.

References

- Ague JJ (2014) Fluid flow in the deep crust. Treatise on geochemistry, 2nd edn. Elsevier, London, pp 203–247
- An SC, Li SG, Liu Z (2018) Modification of the Sm–Nd isotopic system in garnet induced by retrogressive fluids. *J Metamorph Geol* 36:1039–1048
- Ayers JC, Watson EB (1991) Solubility of apatite, monazite, zircon, and rutile in supercritical aqueous fluids with implications for subduction zone geochemistry. *Philos Trans R Soc Lond Ser A Phys Eng Sci* 335:365–375
- Baker J, Matthews A, Matthey D, Rowley D, Xue F (1997) Fluid–rock interactions during ultra-high pressure metamorphism, Dabie Shan, China. *Geochim Cosmochim Acta* 61:1685–1696
- Blichert-Toft J, Albarede F (1997) The Lu–Hf geochemistry of chondrites and the evolution of the mantle–crust system. *Earth Planet Sci Lett* 148:243–258 (**Erratum**, 154, 349)
- Bovay T, Rubatto D, Lanari P (2021) Pervasive fluid–rock interaction in subducted oceanic crust revealed by oxygen isotope zoning in garnet. *Contrib Miner Petrol* 176:55
- Brendebach B, Altmaier M, Rothe J, Neck V, Denecke MA (2007) EXAFS study of aqueous Zr^{IV} and Th^{IV} complexes in alkaline CaCl_2 solutions: $\text{Ca}_3[\text{Zr}(\text{OH})_6]^{4+}$ and $\text{Ca}_4[\text{Th}(\text{OH})_8]^{4+}$. *Inorg Chem* 46:6804–6810
- Caddick MJ, Konopásek J, Thompson AB (2010) Preservation of garnet growth zoning and the duration of prograde metamorphism. *J Petrol* 51:2327–2347
- Carlson WD (2006) Rates of Fe, Mg, Mn, and Ca diffusion in garnet. *Am Miner* 91:1–11
- Carson CJ, Clarke GL, Powell R (2000) Hydration of eclogite, pam peninsula, new caledonia. *J Metamorph Geol* 18:79–90
- Carswell DA, O'Brien PJ, Wilson RN, Zhai M (1997) Thermobarometry of phengite-bearing eclogites in the Dabie Mountains of central China. *J Metamorph Geol* 15:239–252
- Carswell DA, Wilson RN, Zhai M (2000) Metamorphic evolution, mineral chemistry and thermobarometry of schists and orthogneisses hosting ultra-high pressure eclogites in the Dabieshan of central China. *Lithos* 52:121–155
- Castelli D, Rolfo F, Groppo C, Compagnoni R (2007) Impure marbles from the UHP Brossasco-Isasca Unit (Dora–Maira Massif, western Alps): evidence for Alpine equilibration in the diamond stability field and evaluation of the $\text{X}(\text{CO}_2)$ fluid evolution. *J Metamorph Geol* 25:587–603
- Chen B, Jahn B-M, Wei CJ (2002) Petrogenesis of Mesozoic granitoids in the Dabie UHP complex, Central China: trace element and Nd–Sr isotope evidence. *Lithos* 60:67–88
- Chen RX, Zheng YF, Xie LW (2010) Metamorphic growth and recrystallization of zircon: Distinction by simultaneous in-situ analyses of trace elements, U–Th–Pb and Lu–Hf isotopes in zircons from eclogite-facies rocks in the Sulu orogen. *Lithos* 114:132–154
- Chen YX, Zheng YF, Chen RX, Zhang SB, Li QL, Dai MN, Chen L (2011) Metamorphic growth and recrystallization of zircons in extremely ^{18}O -depleted rocks during eclogite-facies metamorphism: evidence from U–Pb ages, trace elements, and O–Hf isotopes. *Geochim Cosmochim Acta* 75:4877–4898
- Chen RX, Zheng YF, Hu ZC (2012) Episodic fluid action during exhumation of deeply subducted continental crust: geochemical constraints from zoisite-quartz vein and host metabasite in the Dabie orogen. *Lithos* 155:146–166
- Chen YX, Zheng YF, Hu ZC (2013) Polyphase growth of accessory minerals during continental collision: geochemical evidence from ultrahigh-pressure metamorphic gneisses in the Sulu orogen. *Lithos* 177:245–267
- Chen YX, Tang J, Zheng YF, Wu YB (2016) Geochemical constraints on petrogenesis of marble-hosted eclogites from the Sulu orogen in China. *Chem Geol* 436:35–53
- Cheng H, Nakamura E, Kobayashi K, Zhou ZY (2007) Origin of atoll garnets in eclogites and implications for the redistribution of trace elements during slab exhumation in a continental subduction zone. *Am Miner* 92:1119–1129
- Cong BL (1996) Ultrahigh-pressure metamorphic rocks in the Dabie-shan-Sulu region of China. Science Press, Beijing, p 224
- Cong BL, Zhai MG, Carswell DA, Wilson RN, Wang QC, Zhao ZY, Windley BF (1995) Petrogenesis of ultrahigh-pressure rocks and their country rocks at Shuanghe in Dabie Shan, Central China. *Eur J Mineral* 7:119–138
- Connolly JAD (2009) The geodynamic equation of state: what and how. *Geochem Geophys Geosyst* 10:Q10014
- Connolly JAD, Galvez ME (2018) Electrolytic fluid speciation by Gibbs energy minimization and implications for subduction zone mass transfer. *Earth Planet Sci Lett* 501:90–102
- Connolly JAD, Trommsdorff V (1991) Petrogenetic grids for metacarbonate rocks: pressure-temperature phase-diagram projection for mixed-volatile systems. *Contrib Miner Petrol* 108:93–105
- Corfu F, Hanchar JM, Hoskin PWO, Kinny P (2003) Atlas of zircon textures. *Zircon* 53:469–500

- Crisp LJ, Berry AJ, Burnham AD, Miller LA, Newville M (2023) The Ti-in-zircon thermometer revised: the effect of pressure on the Ti site in zircon. *Geochim Cosmochim Acta* 360:241–258
- Ebanu M, Nagasaki A (1999) Prograde P–T path of kyanite eclogites from Junan in the Sulu ultrahigh-pressure province, eastern China. *Island Arc* 8:459–474
- El Korh A, Schmidt ST, Ulianov A, Potel S (2009) Trace element partitioning in HP–LT metamorphic assemblages during subduction-related metamorphism, Ile de Groix, France: a Detailed LA-ICPMS Study. *J Petrol* 50:1107–1148
- Faryad SW, Kláková H, Nosál L (2018) Mechanism of formation of atoll garnet during high-pressure metamorphism. *Min Mag* 74:111–126
- Ferriss EDA, Essene EJ, Becker U (2008) Computational study of the effect of pressure on the Ti-in-zircon geothermometer. *Eur J Mineral* 20:745–755
- Ferry JM, Watson EB (2007) New thermodynamic models and revised calibrations for the Ti-in-zircon and Zr-in-rutile thermometers. *Contrib Miner Petrol* 154:429–437
- Fuhrman ML, Lindsley DH (1988) Ternary-feldspar modeling and thermometry. *Am Miner* 73:201–215
- Ganguly J, Cheng W, Chakraborty S (1998) Cation diffusion in aluminosilicate garnets: experimental determination in pyrope-almandine diffusion couples. *Contrib Miner Petrol* 131:171–180
- Gao XY, Zheng YF, Chen YX (2011) U–Pb ages and trace elements in metamorphic zircon and titanite from UHP eclogite in the Dabie orogen: constraints on P–T–t path. *J Metamorph Geol* 29:721–740
- Gao XY, Wang L, Chen YX, Zheng YF, Chen RX, Huang F, Zhang QQ, Ji M, Meng ZY (2019) Geochemical evidence from coesite-bearing jadeite quartzites for large-scale flow of metamorphic fluids in a continental subduction channel. *Geochim Cosmochim Acta* 265:354–370
- Geisler T, Schaltegger U, Tomaschek F (2007) Re-equilibration of zircon in aqueous fluids and melts. *Elements* 3:43–50
- Gerdes A, Zeh A (2009) Zircon formation versus zircon alteration—new insights from combined U–Pb and Lu–Hf in-situ LA–ICP–MS analyses, and consequences for the interpretation of Archean zircon from the Central Zone of the Limpopo Belt. *Chem Geol* 261:230–243
- Giuntoli F, Lanari P, Engi M (2018) Deeply subducted continental fragments—part 1: Fracturing, dissolution-precipitation, and diffusion processes recorded by garnet textures of the central Sesia Zone (western Italian Alps). *Solid Earth* 9:167–189
- Green ECR, Holland TJB, Powell R (2007) An order-disorder model for omphacitic pyroxenes in the system jadeite-diopside-hedenbergite-acmite, with applications to eclogitic rocks. *Am Miner* 92:1181–1189
- Green ECR, White RW, Diener JFA, Powell R, Holland TJB, Palin RM (2016) Activity–composition relations for the calculation of partial melting equilibria in metabasic rocks. *J Metamorph Geol* 34:845–869
- Guiraud M, Powell R, Rebay G (2001) H₂O in metamorphism and unexpected behaviour in the preservation of metamorphic mineral assemblages. *J Metamorph Geol* 19:445–454
- Guo S, Ye K, Chen Y, Liu JB, Mao Q, Ma YG (2012) Fluid–rock interaction and element mobilization in UHP metabasalt: constraints from an omphacite-epidote vein and host eclogites in the Dabie orogen. *Lithos* 136–139:145–167
- Guo S, Ye K, Wu TF, Chen Y, Yang YH, Zhang LM, Liu JB, Mao Q, Ma YG (2013) A potential method to confirm the previous existence of lawsonite in eclogite: the mass imbalance of Sr and LREEs in multistage epidote (Ganghe, Dabie UHP terrane). *J Metamorph Geol* 31:415–435
- Guo S, Su B, John T, Zhao KD, Tang P, Chen Y, Li YB (2022) Boron release and transfer induced by phengite breakdown in subducted impure metacarbonates. *Lithos* 408–409:106548
- Hacker BR, Ratschbacher L, Webb L, Ireland T, Walker D, Dong SW (1998) U/Pb zircon ages constrain the architecture of the ultrahigh-pressure Qinling-Dabie Orogen, China. *Earth Planet Sci Lett* 161:215–230
- Harlov DE, Anczkiewicz R, Dunkley DJ (2023) Metasomatic alteration of zircon at lower crustal P–T conditions utilizing alkali- and F-bearing fluids: trace element incorporation, depletion, and resetting the zircon geochronometer. *Geochim Cosmochim Acta* 352:222–235
- Hermann J (2002) Allanite: thorium and light rare earth element carrier in subducted crust. *Chem Geol* 192:289–306
- Hermann J, Rubatto D (2014) Subduction of continental crust to mantle depth: geochemistry of ultrahigh-pressure rocks. In: Holland HD, Turekian KK (eds) *Treatise on geochemistry*, 2nd edn. Elsevier, Amsterdam, pp 309–340
- Hermann J, Spandler C (2008) Sediment melts at sub-arc depths: an experimental study. *J Petrol* 49:717–740
- Hermann J, Spandler C, Hack A, Korsakov A (2006) Aqueous fluids and hydrous melts in high-pressure and ultra-high pressure rocks: implications for element transfer in subduction zones. *Lithos* 92:399–417
- Holland TJB, Powell R (1991) A compensated Redlich-Kwong (CORK) equation for volumes and fugacities of CO₂ and H₂O in the range 1 bar to 50 kbar and 100–1600 °C. *Contrib Miner Petrol* 109:265–273
- Holland TJB, Powell R (1998) An internally consistent thermodynamic data set for phases of petrological interest. *J Metamorph Geol* 16:309–343
- Holland TJB, Powell R (2011) An improved and extended internally consistent thermodynamic dataset for phases of petrological interest, involving a new equation of state for solids. *J Metamorph Geol* 29:333–383
- Hoover WF, Penniston-Dorland S, Baumgartner L, Bouvier A-S, Dragovic B, Locatelli M, Angiboust S, Agard P (2022) Episodic fluid flow in an eclogite-facies shear zone: Insights from Li isotope zoning in garnet. *Geology* 50:746–750
- Hoskin PWO, Black LP (2000) Metamorphic zircon formation by solid-state recrystallization of protolith igneous zircon. *J Metamorph Geol* 18:423–439
- Hu ZC, Gao S, Liu YS, Hu SH, Chen HH, Yuan HL (2008) Signal enhancement in laser ablation ICP-MS by addition of nitrogen in the central channel gas. *J Anal Spect* 23:1093–1101
- Hu ZC, Liu YS, Gao S, Liu W, Yang L, Zhang W, Tong X, Lin L, Zong KQ, Li M, Chen H, Zhou L (2012) Improved in situ Hf isotope ratio analysis of zircon using newly designed X skimmer cone and Jet sample cone in combination with the addition of nitrogen by laser ablation multiple collector ICP-MS. *J Anal Spect* 27:1391–1399
- Hu ZC, Li XH, Luo T, Zhang W, Crowley J, Li QL, Ling XX, Yang C, Li Y, Feng LP, Xia XP, Zhang SB, Wang ZC, Guo JL, Xu L, Lin J, Liu XM, Bao ZA, Liu YS, Zong KQ, Chen W, Hu SH (2021) Tanz zircon megacrysts: a new zircon reference material for the microbeam determination of U–Pb ages and Zr–O isotopes. *J Anal Spect* 36:2715–2734
- Jackson SE, Pearson NJ, Griffin WL, Belousova EA (2004) The application of laser ablation-inductively coupled plasma-mass spectrometry to in situ U–Pb zircon geochronology. *Chem Geol* 211:47–69
- John T, Klemd R, Gao J, Garbe-Schönberg C-D (2008) Trace-element mobilization in slabs due to non steady-state fluid–rock interaction: constraints from an eclogite-facies transport vein in blueschist (Tianshan, China). *Lithos* 103:1–24

- Kessel R, Schmidt MW, Ulmer P, Pettke T (2005) Trace element signature of subduction-zone fluids, melts and supercritical liquids at 120–180 km depth. *Nature* 437:724–727
- Kohn MJ (2014) Geochemical zoning in metamorphic minerals. In: Holland HD, Turekian KK (eds) *The crust. Treatise on Geochemistry*, vol 4, 2nd edn. Elsevier, Oxford, pp 249–280
- Konrad-Schmolke M, O'Brien PJ, Heidelbach F (2007) Compositional re-equilibration of garnet: the importance of sub-grain boundaries. *Eur J Min* 19:431–438
- Konzett J, Frost DJ (2009) The high P–T stability of hydroxyl-apatite in natural and simplified MORB—an experimental study to 15 GPa with implications for transport and storage of phosphorus and halogens in subduction zones. *J Petrol* 50:2043–2062
- Kovalenko NI, Ryzhenko BN (2009) Comparative study of the solubility of zircon and baddeleyite. *Geochem Int* 47:405–413
- Kulhánek J, Faryad SW, Jedlicka R, Svojtka M (2021) Dissolution and reprecipitation of garnet during eclogite-facies metamorphism; major and trace element transfer during atoll garnet formation. *J Petrol* 62:1–22
- Leake BE, Woolley AR, Arps CES, Birch WD, Gilbert MC, Grice JD, Hawthorne FC, Kato A, Kisch HJ, Krivovichev VG, Linthout K, Laird J, Mandarino JA, Maresch WV, Nickel EH, Rock NMS, Schumacher JC, Smith DC, Stephenson NCN, Ungaretti L, Whittaker EJW, Guo YZ (1997) Nomenclature of amphiboles: report of the subcommittee on amphiboles of the international mineralogical association commission on new minerals and mineral names. *Min Mag* 35:219–246
- Lenting C, Geisler T, Gerdes A, Kooijman E, Scherer EE, Zeh A (2010) The behavior of the Hf isotope system in radiation-damaged zircon during experimental hydrothermal alteration. *Am Miner* 95:1343–1348
- Li SG, Xiao YL, Liou DL, Chen YZ, Ge NJ, Zhang ZQ (1993) Collision of the North China and Yangtze Blocks and formation of coesite-bearing eclogites: timing and processes. *Chem Geol* 109:89–111
- Li SG, Jagoutz E, Chen YZ, Li QL (2000) Sm–Nd and Rb–Sr isotope chronology and cooling history of ultrahigh pressure metamorphic rocks and their country rocks at Shuanghe in the Dabie Mountains, Central China. *Geochim Cosmochim Acta* 64:1077–1093
- Li YL, Zheng YF, Fu B, Zhou JB, Wei CS (2001) Oxygen isotope composition of quartz-vein in ultrahigh-pressure eclogite from dabieshan and implications for transport of high-pressure metamorphic fluid. *Phys Chem Earth (a)* 26:695–704
- Li XP, Zheng YF, Wu YB, Chen FK, Gong B, Li YL (2004) Low-T eclogite in the Dabie terrane of China: petrological and isotopic constraints on fluid activity and radiometric dating. *Contrib Miner Petrol* 148:443–470
- Liu PL, Jin ZM (2022) Metamorphic evolution of a tremolite marble from the Dabie UHP Terrane, China: a Focus on Zircon. *J Earth Sci* 33:493–506
- Liu FL, Liou JG (2011) Zircon as the best mineral for P–T-time history of UHP metamorphism: a review on mineral inclusions and U–Pb SHRIMP ages of zircons from the Dabie-Sulu UHP rocks. *J Asian Earth Sci* 40:1–39
- Liu JB, Ye K, Maruyama S, Cong BL, Fan HR (2001) Mineral inclusions in zircon from gneisses in the ultrahigh-pressure zone of the Dabie Mountains, China. *J Geol* 109:523–535
- Liu XC, Jahn B-m, Dong SW, Li HM, Oberhänsli R (2003) Neoproterozoic granitoid did not record ultrahigh-pressure metamorphism from the Southern Dabieshan of China. *J Geol* 111:719–732
- Liu DY, Jian P, Kröner A, Xu ST (2006a) Dating of prograde metamorphic events deciphered from episodic zircon growth in rocks of the Dabie-Sulu UHP complex, China. *Earth Planet Sci Lett* 250:650–666
- Liu FL, Gerdes A, Liou JG, Xue HM, Liang FH (2006b) SHRIMP U–Pb zircon dating from Sulu-Dabie dolomitic marble, eastern China: constraints on prograde, ultrahigh-pressure and retrograde metamorphic ages. *J Metamorph Geol* 24:569–589
- Liu YS, Hu ZC, Gao S, Günther D, Xu J, Gao CG, Chen HH (2008) In situ analysis of major and trace elements of anhydrous minerals by LA–ICP–MS without applying an internal standard. *Chem Geol* 257:34–43
- Liu YS, Gao S, Hu ZC, Gao CG, Zong KQ, Wang DB (2010) Continental and oceanic crust recycling-induced melt-peridotite interactions in the Trans-North China Orogen: U–Pb dating, Hf isotopes and trace elements in zircons of mantle xenoliths. *J Petrol* 51:537–571
- Liu PL, Wu Y, Chen Y, Zhang JF, Jin ZM (2015) UHP impure marbles from the Dabie Mountains: Metamorphic evolution and carbon cycling in continental subduction zones. *Lithos* 212–215:280–297
- Liu PL, Massonne H-J, Jin ZM, Wu Y, Zhang JF (2017) Diopside, apatite, and rutile in an ultrahigh pressure impure marble from the Dabie Shan, eastern China: a record of eclogite-facies metasomatism during exhumation. *Chem Geol* 466:123–139
- Liu PL, Massonne H-J, Harlov DE, Jin ZM (2019) High-pressure fluid–rock interaction and mass transfer during exhumation of deeply subducted rocks: insights from an eclogite-vein system in the ultrahigh-pressure terrane of the Dabie Shan, China. *Geochem Geophys Geosyst* 20:5786–5817
- Ludwig KR (2003) *ISOPLLOT 3.00: a geochronological toolkit for Microsoft excel*. Berkeley Geochronology Center Special Publication, p 39
- Maffei A, Ferrando S, Connolly JAD, Groppo C, Frezzotti ML, Castelli D (2021) Thermodynamic analysis of HP–UHP fluid inclusions: the solute load and chemistry of metamorphic fluids. *Geochim Cosmochim Acta* 315:207–229
- Martin LAJ, Duchêne S, Deloule E, Vanderhaeghe O (2008) Mobility of trace elements and oxygen in zircon during metamorphism: consequences for geochemical tracing. *Earth Planet Sci Lett* 267:161–174
- Martin LAJ, Ballèvre M, Boulvais P, Halfpenny A, Vanderhaeghe O, Duchêne S, Deloule E (2011) Garnet re-equilibration by coupled dissolution-precipitation: evidence from textural, major element and oxygen isotope zoning of ‘cloudy’ garnet. *J Metamorph Geol* 29:213–231
- Martin LAJ, Hermann J, Gauthiez-Putallaz L, Whitney DL, Vitale Brovarone A, Fornash KF, Evans NJ (2014) Lawsonite geochemistry and stability—implication for trace element and water cycles in subduction zones. *J Metamorph Geol* 32:455–478
- Massonne H-J (2009) Hydration, dehydration, and melting of metamorphosed granitic and dioritic rocks at high- and ultrahigh-pressure conditions. *Earth Planet Sci Lett* 288:244–254
- Massonne H-J (2012) Formation of Amphibole and Clinozoisite-Epidote in Eclogite owing to Fluid Infiltration during Exhumation in a Subduction Channel. *J Petrol* 53:1969–1998
- Mulcahy SR, King RL, Vervoort JD (2009) Lawsonite Lu–Hf geochronology: a new geochronometer for subduction zone processes. *Geology* 37:987–990
- Nosenzo F, Manzotti P, Robyr M (2023) H₂O budget and metamorphic re-equilibration in polycyclic rocks as recorded by garnet textures and chemistry. *Lithos* 452–453:107230
- Nowell GM, Kempton PD, Noble SR, Fitton JG, Saunders AD, Mahoney JJ, Taylor RN (1998) High precision Hf isotope measurements of MORB and OIB by thermal ionisation mass spectrometry: insights into the depleted mantle. *Chem Geol* 149:211–233
- Okay AI, Shutong X, Sengör AMC (1989) Coesite from the Dabie Shan eclogites, central China. *Eur J Mineral* 1:595–598

- Poli S, Schmidt MW (2004) Experimental subsolidus studies on epidote minerals. *Rev Mineral Geochem* 56:171–195
- Proyer A (2003) The preservation of high-pressure rocks during exhumation: metagranites and metapelites. *Lithos* 70:183–194
- Putnis A (2002) Mineral replacement reactions: from macroscopic observations to microscopic mechanisms. *Mineral Mag* 66:689–708
- Putnis CV, Mezger K (2004) A mechanism of mineral replacement: isotope tracing in the model system KCl–KBr–H₂O. *Geochim Cosmochim Acta* 68:2839–2848
- Rolfo F, Compagnoni R, Wu WP, Xu ST (2004) A coherent lithostratigraphic unit in the coesite–eclogite complex of Dabie Shan, China: geologic and petrologic evidence. *Lithos* 73:71–94
- Rubatto D (2002) Zircon trace element geochemistry: partitioning with garnet and the link between U–Pb ages and metamorphism. *Chem Geol* 184:123–138
- Rubatto D (2017) Zircon: the metamorphic mineral. *Rev Mineral Geochem* 83:261–296
- Rubatto D, Hermann J (2003) Zircon formation during fluid circulation in eclogites (Monviso, Western Alps): implications for Zr and Hf budget in subduction zones. *Geochim Cosmochim Acta* 67:2173–2187
- Rubatto D, Hermann J, Berger A, Engi M (2009) Protracted fluid-induced melting during Barrovian metamorphism in the Central Alps. *Contrib Miner Petrol* 158:703–722
- Rumble D, Wang QC, Zhang RY (2000) Stable isotope geochemistry of marbles from the coesite UHP terrains of Dabieshan and Sulu, China. *Lithos* 52:79–95
- Sassi R, Harte B, Carswell DA, Yujing H (2000) Trace element distribution in Central Dabie eclogites. *Contrib Miner Petrol* 139:298–315
- Schmid R, Franz L, Oberhänsli R, Dong SW (2000) High-Si phengite, mineral chemistry and P–T evolution of ultra-high-pressure eclogites and calc-silicates from the Dabie Shan, eastern China. *Geol J* 35:187–207
- Schmidt MW, Poli S (1998) Experimentally based water budgets for dehydrating slabs and consequences for arc magma generation. *Earth Planet Sci Lett* 163:361–379
- Schmidt C, Rickers K, Wirth R, Nasdala L, Hanchar JM (2006) Low-temperature Zr mobility: An in situ synchrotron-radiation XRF study of the effect of radiation damage in zircon on the element release in H₂O + HCl ± SiO₂ fluids. *Am Miner* 91:1211–1215
- Schmidt A, Weyer S, Mezger K, Scherer EE, Xiao YL, Hoefs J, Brey GP (2008) Rapid eclogitisation of the Dabie-Sulu UHP terrane: constraints from Lu–Hf garnet geochronology. *Earth Planet Sci Lett* 273:203–213
- Sláma J, Košler J, Condon DJ, Crowley JL, Gerdes A, Hanchar JM, Horstwood MSA, Morris GA, Nasdala L, Norberg N, Schaltegger U, Schoene B, Tubrett MN, Whitehouse MJ (2008) Plešovice zircon—a new natural reference material for U–Pb and Hf isotopic microanalysis. *Chem Geol* 249:1–35
- Smit MA, Bröcker M, Scherer EE (2008) Aragonite and magnesite in eclogites from the Jaeren nappe, SW Norway: disequilibrium in the system CaCO₃–MgCO₃ and petrological implications. *J Metamorph Geol* 26:959–979
- Söderlund U, Patchett PJ, Vervoort JD, Isachsen CE (2004) The ¹⁷⁶Lu decay constant determined by Lu–Hf and U–Pb isotope systematics of Precambrian mafic intrusions. *Earth Planet Sci Lett* 219:311–324
- Spandler C, Pirard C (2013) Element recycling from subducting slabs to arc crust: a review. *Lithos* 170–171:208–223
- Spandler C, Hermann J, Arculus R, Mavrogenes J (2003) Redistribution of trace elements during prograde metamorphism from lawsonite blueschist to eclogite facies; implications for deep subduction-zone processes. *Contrib Miner Petrol* 146:205–222
- Spandler C, Mavrogenes J, Hermann J (2007) Experimental constraints on element mobility from subducted sediments using high-P synthetic fluid/melt inclusions. *Chem Geol* 239:228–249
- Stepanov AS, Hermann J, Rubatto D, Korsakov AV, Danyushevsky LV (2016) Melting history of an ultrahigh-pressure paragneiss revealed by multiphase solid inclusions in garnet, Kokchetav Massif, Kazakhstan. *J Petrol* 57:1531–1554
- Sun SS, McDonough WF (1989) Chemical and isotopic systematics of oceanic basalts: implications for mantle composition and processes. *Geol Soc Lond Spec Publ* 42:313–345
- Taguchi T, Enami M, Kouketsu Y (2016) Prograde evolution of Sulu UHP metamorphic rock in Yangzhuang, Junan region, deduced by combined Raman and petrological studies. *J Metamorph Geol* 34:683–696
- Tailby ND, Walker AM, Berry AJ, Hermann J, Evans KA, Mavrogenes JA, O'Neill HSC, Rodina IS, Soldatov AV, Rubatto D, Sutton SR (2011) Ti site occupancy in zircon. *Geochim Cosmochim Acta* 75:905–921
- Vervoort JD, Patchett PJ, Blichert-Toft J, Albarede F (1999) Relationship between Lu–Hf and Sm–Nd isotopic systems in the global sedimentary system. *Earth Planet Sci Lett* 168:79–99
- Vho A, Rubatto D, Lanari P, Giuntoli F, Regis D, Hermann J (2020) Crustal reworking and hydration: insights from element zoning and oxygen isotopes of garnet in high-pressure rocks (Sesia Zone, Western Alps). *Contrib Miner Petrol* 175:109
- Wang X, Liou JG (1993) Ultrahigh-pressure metamorphism of carbonate rocks in the Dabie Mountains, Central China. *J Metamorph Geol* 11:575–585
- Warr LN (2021) IMA–CNMNC approved mineral symbols. *Mineral Mag* 85:291–320
- Watson EB, Wark DA, Thomas JB (2006) Crystallization thermometers for zircon and rutile. *Contrib Miner Petrol* 151:413–433
- Wawzenitz N, Romer RL, Grasemann B, Morales LG (2019) Pre-UHP titanite archives pro- and retrograde episodes of fluid-marble-interaction (Dabie Shan UHP unit, China). *Lithos* 350–351:105232
- Wei CJ, Duan ZZ (2018) Phase relations in metabasic rocks: constraints from the results of experiments, phase modelling and ACF analysis. *Geol Soc Lond Spec Publ* 474:25–45
- Wei CJ, Qian JH, Tian ZL (2013) Metamorphic evolution of medium-temperature ultra-high pressure (MT-UHP) eclogites from the South Dabie orogen, Central China: an insight from phase equilibrium modelling. *J Metamorph Geol* 31:755–774
- White RW, Powell R, Holland TJB, Johnson TE, Green ECR (2014) New mineral activity–composition relations for thermodynamic calculations in metapelitic systems. *J Metamorph Geol* 32:261–286
- Whitehouse MJ, Platt JP (2003) Dating high-grade metamorphism—constraints from rare-earth elements in zircon and garnet. *Contrib Miner Petrol* 145:61–74
- Wilke M, Schmidt C, Dubraille J, Appel K, Borchert M, Kvashnina K, Manning CE (2012) Zircon solubility and zirconium complexation in H₂O + Na₂O + SiO₂ ± Al₂O₃ fluids at high pressure and temperature. *Earth Planet Sci Lett* 349–350:15–25
- Wu YB, Zheng YF, Zhao ZF, Gong B, Liu XM, Wu FY (2006) U–Pb, Hf and O isotope evidence for two episodes of fluid-assisted zircon growth in marble-hosted eclogites from the Dabie orogen. *Geochim Cosmochim Acta* 70:3743–3761
- Wu YB, Gao S, Liu XC, Wang J, Peng M, Gong HJ, Yuan HL (2011) Two-stage exhumation of ultrahigh-pressure metamorphic rocks from the Western Dabie Orogen, Central China. *J Geol* 119:15–31
- Xiong JW, Chen YX, Zhou K, Schertl H-P, Zheng YF, Huang F, Xia XP, Chen ZW (2021) Fe and O isotopes in coesite-bearing jadeite quartzite from the Western Alps record multistage fluid–rock

- interactions in a continental subduction zone. *Geochim Cosmochim Acta* 312:1–24
- Yakymchuk C, Kirkland CL, Clark C (2018) Th/U ratios in metamorphic zircon. *J Metamorph Geol* 36:715–737
- Yu J, Glorie S, Martin H, Simpson A, Gilbert S, Szilas K, Roberts N, Pawley M, Cheng YB (2024) Laser ablation (in situ) Lu–Hf geochronology of epidote group minerals. *Contrib Miner Petrol* 179:62
- Zeh A, Gerdes A (2014) HFSE (High Field Strength Elements)-transport and U–Pb–Hf isotope homogenization mediated by Ca-bearing aqueous fluids at 2.04 Ga: constraints from zircon, monazite, and garnet of the Venetia Klippe, Limpopo Belt, South Africa. *Geochim Cosmochim Acta* 138:81–100
- Zhang HF, Gao S, Zhong ZQ, Zhang BR, Zhang L, Hu SG (2002) Geochemical and Sr–Nd–Pb isotopic compositions of Cretaceous granitoids: constraints on tectonic framework and crustal structure of the Dabieshan ultrahigh-pressure metamorphic belt, China. *Chem Geol* 186:281–299
- Zhang ZM, Xiao YL, Liu FL, Liou JG, Hoefs J (2005) Petrogenesis of UHP metamorphic rocks from Qinglongshan, southern Sulu, east-central China. *Lithos* 81:189–207
- Zhang ZM, Shen K, Sun WD, Liu YS, Liou JG, Shi C, Wang JL (2008) Fluids in deeply subducted continental crust: petrology, mineral chemistry and fluid inclusion of UHP metamorphic veins from the Sulu orogen, eastern China. *Geochim Cosmochim Acta* 72:3200–3228
- Zhang ZM, Schertl H-P, Wang JL, Shen K, Liou JB (2009) Source of Coesite inclusions within inherited magmatic zircon from Sulu UHP Rocks, Eastern China, and their bearing for fluid–rock interaction and SHRIMP dating. *J Metamorph Geol* 27:317–333
- Zhao YJ, Wu YB, Liu XC, Gao S, Wang H, Zheng JP, Yang SH (2016) Distinct zircon U–Pb and O–Hf–Nd–Sr isotopic behaviour during fluid flow in UHP metamorphic rocks: evidence from metamorphic veins and their host eclogite in the Sulu Orogen, China. *J Metamorph Geol* 34:343–362
- Zheng YF, Fu B, Gong B, Li L (2003) Stable isotope geochemistry of ultrahigh pressure metamorphic rocks from the Dabie-Sulu orogen in China: implications for geodynamics and fluid regime. *Earth Sci Rev* 62:105–161
- Zheng YF, Wu YB, Chen FK, Gong B, Li L, Zhao ZF (2004) Zircon U–Pb and oxygen isotope evidence for a large-scale ^{18}O depletion event in igneous rocks during the Neoproterozoic. *Geochim Cosmochim Acta* 68:4145–4165
- Zheng YF, Zhou JB, Wu YB, Xie Z (2005a) Low-grade metamorphic rocks in the Dabie-Sulu orogenic belt: a passive-margin accretionary wedge deformed during continent subduction. *Int Geol Rev* 47:851–871
- Zheng YF, Wu YB, Zhao ZF, Zhang SB, Xu P, Wu FY (2005b) Metamorphic effect on zircon Lu–Hf and U–Pb isotope systems in ultrahigh-pressure eclogite-facies metagranite and metabasite. *Earth Planet Sci Lett* 240:378–400
- Zheng YF, Gao TS, Wu YB, Gong B, Liu XM (2007) Fluid flow during exhumation of deeply subducted continental crust: zircon U–Pb age and O-isotope studies of a quartz vein within ultrahigh-pressure eclogite. *J Metamorph Geol* 25:267–283
- Zheng YF, Gong B, Zhao ZF, Wu YB, Chen FK (2008) Zircon U–Pb age and o isotope evidence for Neoproterozoic low- ^{18}O magmatism during supercontinental rifting in South China: Implications for the snowball earth event. *Am J Sci* 308:484–516
- Zheng YF, Chen RX, Zhao ZF (2009) Chemical geodynamics of continental subduction-zone metamorphism: Insights from studies of the Chinese Continental Scientific Drilling (CCSD) core samples. *Tectonophysics* 475:327–358
- Zong KQ, Klemd R, Yuan Y, He ZY, Guo JL, Shi XL, Liu YS, Hu ZC, Zhang ZM (2017) The assembly of Rodinia: the correlation of early Neoproterozoic (ca. 900 Ma) high-grade metamorphism and continental arc formation in the southern Beishan Orogen, southern Central Asian Orogenic Belt (CAOB). *Precamb Res* 290:32–48

Publisher's Note Springer Nature remains neutral with regard to jurisdictional claims in published maps and institutional affiliations.

Springer Nature or its licensor (e.g. a society or other partner) holds exclusive rights to this article under a publishing agreement with the author(s) or other rightsholder(s); author self-archiving of the accepted manuscript version of this article is solely governed by the terms of such publishing agreement and applicable law.